Skoltech

Skolkovo Institute of Science and Technology

Skolkovo Institute of Science and Technology

RATIONAL DESIGN OF SINGLE-WALLED CARBON NANOTUBE FILMS FOR TRANSPARENT ELECTRONICS

Doctoral Thesis

by

DANIIL A. ILATOVSKII

DOCTORAL PROGRAM IN MATERIALS SCIENCE AND ENGINEERING

Supervisor
Professor Albert G. Nasibulin

Co-advisor
Assistant Professor Dmitry V. Krasnikov

Moscow - 2023

I hereby declare that the work presented in this thesis was carried out by myself at Skolkovo Institute of Science and Technology, Moscow, except where due acknowledgment is made and has not been submitted for any other degree.

Candidate (Daniil A. Ilatovskii)

Supervisor (Professor Albert G. Nasibulin)

Co-advisor (Assistant Professor Dmitry V. Krasnikov)

Abstract

Over the past three decades, single-walled carbon nanotubes (SWCNTs) have shown significant potential for advanced materials used in applications such as optoelectronics, photovoltaics, and wearable electronics. Precise control of SWCNT properties is crucial for further application in next-generation devices. This study aims to promote the optoelectronic performance of SWCNT films at the deposition and post-deposition stages of the material fabrication.

The first approach utilizes the photophoretic motion of SWCNTs in the aerosol state to control their deposition through light irradiation. The positive photophoretic force, a phenomenon demonstrated for the first time with small bundles of aerosolized SWCNTs, drives particle motion resulting in their deposition. This method enables the deposition of small bundles of nanotubes as well as interconnected SWCNT networks on a substrate. SWCNTs consistently exhibit efficient deposition over time, making depositing films with a desired density convenient and reproducible. The efficiency of the process was around 10% for deposition by LED irradiation. An intriguing correlation was discovered between the spectrum of the irradiation source and the resulting structure of the deposited SWCNT films, attributed to the partial selectivity of photophoretic motion based on their chirality.

The second approach introduces a novel, straightforward method for coating SWCNTs with V_2O_5 through a simple spin-coating process conducted under ambient conditions. This mechanism involves the hydrolysis of a V_2O_5 precursor (vanadyl triisopropoxide), followed by polycondensation directly on the surface of carbon

3

nanotubes in ambient conditions. The resulting nanometer-thick oxide layer was found to be amorphous, featuring a work function of 4.6 eV. Subsequent heating to temperatures between 500 and 600⁰C enabled the material to recrystallize, achieving a work function of 5.8 eV. The feasibility of this approach was validated by achieving stable and efficient outcomes in the transparent electrode performance.

Finally, we outline the strategy for advancing research and development in transparent conductors through the application of "rational design." This approach offers opportunities to achieve the theoretical performance of transparent conductive films. The fundamental limit for sheet resistances was found at 14 and 22 $\mu\Omega$/sq at 90% transmittance for 1D- and 2D conductive SWCNT films, respectively, revealing a huge potential in the field of transparent conductive films based on SWCNTs.

Publications

1. **Ilatovskii, D. A.**, Gilshtein, E. P., Glukhova, O. E., & Nasibulin, A. G. **(2022)**. Transparent Conducting Films Based on Carbon Nanotubes: Rational Design toward the Theoretical Limit. *Advanced Science*, 2201673.

2. **Ilatovskii, D. A.**, Krasnikov, D. V., Goldt, A. E., Mousavihashemi, S., Sainio, J., Khabushev, E. M., Alekseeva, A. A., Luchkin, S. Yu., Vinokurov, Z. S., Shmakov, A. N., Elakshar, A., Kallio, T., & Nasibulin, A. G. **(2023)**. Robust method for V_2O_5 coating of carbon nanotubes for next-generation transparent electrodes and Li-ion batteries. *RSC Advances*, 13, 25817.

3. **Ilatovskii, D. A.**, Krasnikov, D. V., Kopylova, D. S., Davletkhanov, A. I., Gladush, Yu. G., Kondrashov, V. A., Afinogenov, B. I., Maksimov, F. M., Barulin, A., Burdin, V. V., Chernov, A. I., & Nasibulin, A. G. (**2023**). Photophoretic Deposition and Separation of Aerosol-Synthesized Single-Walled Carbon Nanotubes. *Carbon*, accepted 09.12.2023.

4. Mitin, D., Berdnikov, Y., Vorobyev, A., Mozharov, A., Raudik, S., Koval, O., Neplokh, V., Moiseev, E., **Ilatovskii D. A.**, Nasibulin A. G. & Mukhin, I. (**2020**). Optimization of optoelectronic properties of patterned single-walled carbon nanotube films. *ACS Applied Materials & Interfaces*, *12*(49), 55141-55147.

5. Neplokh, V., Kochetkov, F. M., Deriabin, K. V., Fedorov, V. V., Bolshakov, A. D., Eliseev, I. E., Mikhailovskii, V. Yu., **Ilatovskii, D. A.**, Krasnikov, D. V., Tchernycheva, M., Cirlin, G. E., Nasibulin A. G. & Islamova, R. M. (**2020**). Modified silicone rubber for fabrication and contacting of flexible suspended membranes of n-/p-GaP nanowires with a single-walled carbon nanotube transparent contact. *Journal of Materials Chemistry C*, 8(11), 3764-3772.

Author Contribution

Publication 1. The author performed most of the work on the scientific review and wrote the manuscript.

Publication 2. The author performed most of the research: produced the material, characterized it, and tested it as a transparent conductor; wrote the manuscript.

Publication 3. The author performed most of the research: developed the theoretical model, carried out the photophoretic deposition of the samples, and characterized them; wrote the manuscript.

Publication 4. The author manufactured the samples of initial SWCNT thin-film electrodes for further patterning and wrote the methodology of the development for the manuscript.

Publication 5. The author manufactured the free-standing SWCNT electrodes for further transfer on the membranes; and wrote the methodology of the development for the manuscript.

Acknowledgments

I thank my supervisor prof. Albert G. Nasibulin and co-advisor asst. prof. Dmitry V. Krasnikov for explaining to me, how scientific activities should be carried out, as well as for giving me their support, help, and guidance. I am also grateful to the people of Laboratory of Nanomaterials (SkolTech) for being a friendly and comfortable society, providing the most comfortable working atmosphere. Finally, I am thankful to my family – they helped me in all endeavors and any situation.

List of Symbols and Abbreviations

ASE – Amplified Spontaneous Emission

CVD – Chemical Vapor Deposition

DC – Direct Current

FET – Field-Effect Transistor

FoM – Figure of Merit

ITO – Indium-Tin Oxide

LED – Light-emitting diode

PEDOT:PSS – (poly(3,4- ethylene dioxythiophene) doped with poly(styrene sulfonate)

PL – photoluminescence

RBM – Radial Breathing Modes

RH – Relative Humidity

SWCNT – Single-Walled Carbon Nanotube

TCF – Transparent Conductive Film

VTIP – Vanadyl Triisopropoxide

Table of Contents

1. Introduction

Since the beginning of the 2000s, thin films based on single-walled carbon nanotubes (SWCNTs) have become a promising material for modern electronics. A high number of investigations were dedicated to solar devices, organic light-emitting diodes, liquid crystal displays, *etc.*, including transparent conductive film (TCF) as a key element [1]. Among the companies utilizing SWCNT-based electronics are CHASM, Cnano, LG, and Arkema; meanwhile "Canatu Ltd." (Finland), "Timesnano" (China), and "OCSiAl" (Luxembourg/Russia) mainly specialize in SWCNT commercialization. This fact is not surprising – SWCNTs have advantages providing the highest priority among the other materials for TCF production: low refractive index, spectral uniformity, high chemical and physical stability, mechanical flexibility, and almost unlimited source of renewable raw material [1–5]. To employ SWCNTs and their assemblies (films, aerogels, forests, *etc.*) for advanced applications, the properties of nanotubes, such as conductivity, the ratio of semiconducting to metallic species, and the presence of a specific ordered structure, should fit certain requirements. In particular, the key problem of transparent electronics is finding an optimal trade-off between the highest possible electric conductivity and the highest transmittance in the visible range of wavelengths [6,7]. Tuning the properties may be executed at different steps of production of SWCNT film devices: i) synthesis, ii) deposition, and iii) modification of pristine films.

The synthesis approach addresses the properties of individual carbon nanotubes: changes their length, and diameter, and regulates the presence of impurities and defects in a lattice to affect the properties of the resulting films. This is a wide stand-alone topic for

investigations and a lot of effort is put into the optimization of synthesis conditions for tailoring required properties. The novel tendency here is to apply smart technologies for predictions of SWCNT properties, such as machine learning and artificial neural networks [8,9]. However, the improvements in optoelectronic performance have slowed down over the last years and it is necessary to develop the ideas of deposition and rational design (complex modification) of SWCNT films for tuning the properties of SWCNT thin films.

Deposition is one of the post-synthesis modification approaches that deals with the morphology of the resulting film. In the context of SWCNT synthesis using the aerosol chemical vapor deposition method (as employed in this thesis), the dry transfer method is the most convenient [10]. Here, SWCNT networks are initially collected at the reactor outlet on a filter and subsequently transferred onto various substrates by applying pressure between the filter and the substrate. However, this method does not address the challenge of selectively depositing SWCNTs based on their chirality or metallicity. Photophoretic deposition presents a promising solution to this issue. It harnesses the phenomenon of light-induced motion [11], with the velocity of motion depending on the chirality of SWCNTs. This property makes photophoretic deposition a potential solution for achieving chirality-selective SWCNT deposition.

Adsorption doping stands out as a highly effective technique for enhancing the performance of transparent electrodes. Each atom in a SWCNT resides on the surface, and the presence of any impurity has a significant impact on its electronic structure. This influence extends to factors such as the concentration of charge carriers and the position

of the Fermi level [1]. The most significant enhancement in conductivity for carbon nanotubes has been realized through the utilization of dopants, including HNO_3, $HAuCl_4$, and $AuCl_3$ [12]. Regrettably, the introduction of these dopants, while improving conductivity, consistently leads to a drawback: poor time stability in the optoelectronic properties of the doped SWCNTs due to dopant desorption or decomposition [13,14]. To address this issue, it is necessary to apply alternative doping materials. Stable inorganic compounds that serve the dual purpose of doping and protecting are highly promising candidates.

The rational design of TCFs can be viewed as an approach to either creating a composite TCF with superior properties compared to its components or designing a specific conductive geometry that offers high conductivity and transparency. This strategy could potentially overcome the trade-off between conductivity and transmittance in SWCNT-based TCFs by establishing highly conductive paths while maintaining overall high film transparency.

The purposes of **deposition, doping, and rational design** are interconnected with the overarching goal of **improving the optoelectronic performance of SWCNT films for next-generation electronics**. This involves optimizing various stages of film fabrication and addressing challenges in selective SWCNT deposition based on chirality or metallicity to control film properties. Doping focuses on identifying materials that enhance conductivity and ensure long-term stability in optoelectronic properties. Rational design influences film morphology during deposition and overall structure in post-deposition stages, all aimed at achieving the best optoelectronic performance.

2. Scientific Background

2.1 Fabrication of SWCNT-Based Transparent Conductive Films

2.1.1 Alternative Materials for TCF Production

Currently, transparent conducting films is a highly important topic of Materials Science, because they are applied in the production of modern electronics like solar cells [15–20], organic light-emitting diodes [21–25], liquid crystal displays [26–28], touch screens [29–31], wearable devices [32–34]. Approximately 75% of electronic devices that use transparent conductors rely on indium tin oxide (ITO). Despite its outstanding optoelectronic capabilities, the market is actively seeking a suitable alternative. Emerging electronic trends demand a flexible form factor, a feature ITO lacks due to its fragility. Additional drawbacks of ITO include a high refractive index, optical haze, uneven spectral transmission, limited chemical stability, and a depleted supply of raw materials.

SWCNT thin films represent a highly promising candidate for TCF fabrication. SWCNTs demonstrate exceptional ballistic electrical conductivity, superior chemical stability, and remarkable strength and mechanical flexibility [35]. The prospects of alternative materials, which are metal oxides, conducting polymers, metals, and graphene, barely can compete with carbon nanotubes. Transparent conducting metal oxides (ZnO, TiO_2, SnO_2) [36–38] have the same limitations as ITO: they are fragile, possess high refraction and poor stability [39–41]. Conducting polymers, particularly (poly(3,4-ethylene dioxythiophene) doped with poly(styrene sulfonate) [PEDOT:PSS], do not provide stable optoelectronic characteristics, so their applicability is limited [42]. Metals as transparent conductors have three form factors: thin films [43], microgrids [44], and

nanowires [45]. In general, their production is a multi-step and energy-consuming process (thin films) [46], while they possess poor adhesion to substrates (thin films and nanowires) [47,48]. Their prospects are also narrowed because of high roughness and ununiformed electric fields (microgrids, nanowires) [48–51]. Graphene (a 2D allotrope of carbon) is a perspective for TCF production thanks to high transmittance, but due to synthesis peculiarities it forms small grains and requires a complex transfer procedure, which results in the appearance of electric junctions and defects decreasing final conductivity [52,53]. On the other hand, TCFs constructed from SWCNT films offer outstanding optical characteristics, including minimal haze, low reflectivity, and exceptional color contrast.

2.1.2 Quality Factors of TCFs

TCFs are typically manufactured with varying thicknesses, resulting in different levels of transparency and conductivity, depending on the specific demand, method, and materials used. To effectively assess and compare the performance of various TCF materials, it is necessary to introduce a figure of merit (FoM) or quality factor. This FoM is calculated based on key film properties, including transmittance (T) and sheet resistance (R_s), and is applicable across different film thicknesses. Transmittance represents the intensity ratio between the incident radiation (I_0) and the transmitted radiation (I):

$$T = \frac{I}{I_0} = e^{-\alpha t}.$$

(2.1)

t (cm) is the thickness of the material, α (cm^{-1}) is the optical absorption coefficient. Sheet resistance at direct current (dc) is a film conductivity normalized by its thickness and can be defined as:

$$R_s = \frac{1}{\sigma_{dc} \cdot t},$$ (2.2)

where σ_{dc} ($\Omega^{-1} \cdot$cm^{-1}) is the dc conductivity. R_s is expressed in Ω sq^{-1}, illustrating its invariability to any size of a square surface.

The most representative [1] FoM was derived based on the Beer-Lambert law, taking into account film reflectance, which was proposed by Gordon [54] and by Kaskela et al. [10]:

$$FoM = -\frac{1}{log(T+Ref) \cdot R_s}.$$ (2.3)

Equation 2.3 represents a thickness-independent relationship that is well-suited for comparing TCFs with varying transmittance and conductivity characteristics. By employing this equation, we can also determine an equivalent sheet resistance, which is the sheet resistance corresponding to a specific transmittance level, such as $T = 90\%$ [55]:

$$R_{90} = -\frac{log(T+Ref) \cdot R_s}{log(10/9)}.$$ (2.4)

The value derived from Equation 2.4 can be readily compared to established industrial TCF standards. For instance, the equivalent sheet resistance of ITO on a glass substrate is approximately 10 Ω sq^{-1}, while on PET the equivalent sheet resistance is 100 Ω sq^{-1}. In the thesis, we utilize Equation 2.4 to assess and compare various TCFs produced from SWCNTs, as well as to estimate their underlying fundamental constraints, ensuring clarity in our analysis.

2.1.3 Wet and Dry Methods

The methods employed to fabricate SWCNT-based transparent electrodes can be categorized into two main groups: wet and dry techniques. This classification depends on the condition of the surrounding media for the SWCNTs (**Fig. 2.1**).

The wet approach involves collecting SWCNTs in a powdered form, which must first undergo purification to remove amorphous carbon and other impurities (**Fig. 2.1a**). SWCNTs are dispersed through ultrasound treatment in a surfactant solution, followed by a centrifugation step to eliminate larger aggregates. Once a stable dispersion is achieved, SWCNTs are deposited onto a substrate using one of the conventional techniques, such as vacuum filtration, spray/spin/dip coating, Langmuir–Blodgett deposition, or Mayer rod coatings [1,7]. To enhance the optoelectronic performance of SWCNT films, it is crucial to establish a percolated SWCNT network by effectively removing the surfactant material from and between the SWCNTs.

The initial demonstration of the wet approach for producing carbon nanotube-based TCFs was conducted by Wu *et al.* in 2004 [56]. This pioneering work detailed a method involving the filtration of a nanotube suspension, followed by the removal of surfactants and the dissolution of the filter membrane. The resulting thin films showcased a sheet resistance of 30 Ω sq^{-1} at 70% transmittance (with R_{90} = 101 Ω sq^{-1}). A limitation of the wet process is that the dispersion of SWCNTs and the associated chemical treatment typically introduce defects in the nanotubes. Moreover, complete elimination of the dispersion agents from the surface of SWCNTs is a complex task, and these residues can decrease the optoelectronic performance of the resulting films. Usually, SWCNT-

based TCFs produced by this method rarely possess equivalent sheet resistance lower than 100 Ω sq^{-1} even after post-synthesis treatment [1,7], which can be avoided by the means of the dry method.
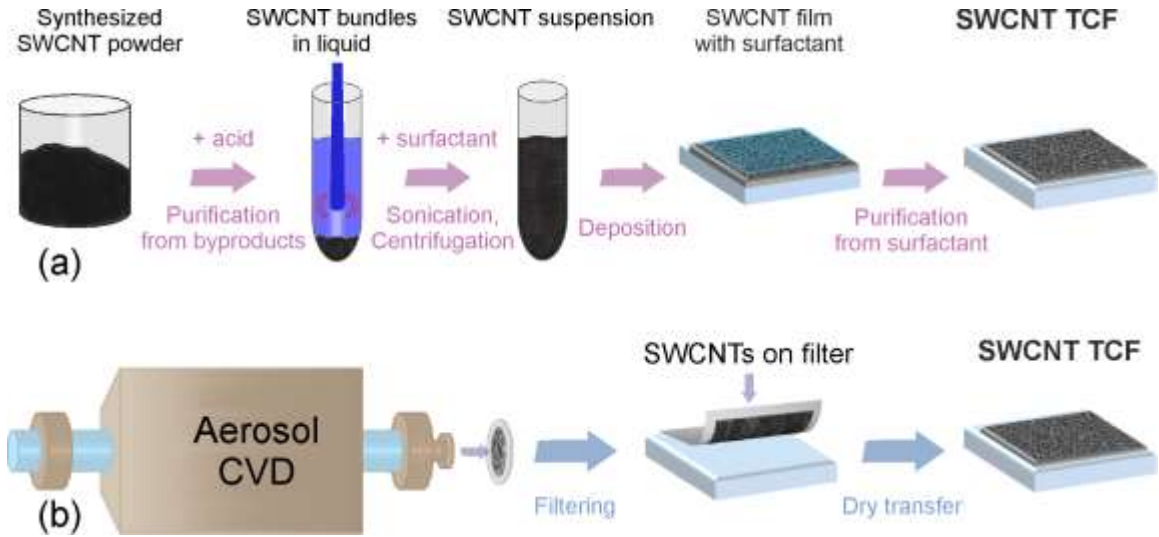
Figure 2.1. Schematic visualization of wet (a) and dry (b) processes for production of transparent conductors based on SWCNTs. Reproduced with permission [1]. Copyright 2022, Wiley.

The dry approach relies on a floating catalyst (aerosol-based) chemical vapor deposition (CVD) method, eliminating the need for liquid media [57]. SWCNTs are formed on catalyst particles suspended in the gas phase and typically collected downstream of the reactor as a self-assembled film comprising randomly oriented SWCNTs on a filter. The fabrication of transparent electrodes using aerosol CVD synthesis was first demonstrated in 2007 [58]. These SWCNT films were transferred from the filter onto a polyethylene substrate using thermal compression, facilitating the adhesion of even shorter-length SWCNTs. The first transparent conductive films (TCFs)

with promising optoelectrical properties were successfully produced in 2010 [10]. The researchers demonstrated a technique for fine-tuning the optoelectronic characteristics of thin SWCNT films by varying bundle lengths during the growth process, achieving an equivalent resistance value of $R_{90} = 110 \ \Omega \ \text{sq}^{-1}$.

This method involves fewer technological steps, resulting in SWCNT films with fewer impurities compared to the wet technique. However, it's important to note that some synthesis byproducts, such as amorphous carbon and residual catalyst particles, almost always appear in these films. This has spurred research into purification methods, including laser treatment and resistive heating of the freestanding SWCNT films, to improve the film quality [59,60]. The conductivity of TCFs is significantly influenced by the characteristics of the synthesized SWCNTs, including their diameter, length, the presence of defects, and surface byproducts [61,62]. High-quality pristine SWCNT films exhibit equivalent sheet resistance values above $R_{90} = 250 \ \Omega \ \text{sq}^{-1}$ [12] which can be noticeably reduced to around 40 Ω sq^{-1} and less by the means of post-synthesis modification [8,63–65]. Among the research papers that assess SWCNT-based transparent conductors, which achieve an equivalent resistance of less than 120 Ω sq^{-1}, the highest performance is reached in the case of dry method utilization [1].

Thus, the most promising approach for SWCNT-based TCF production is the dry method, because it provides the best values for optoelectronic performance. In turn, it requires the utilization of extra techniques after the synthesis step to achieve the highest performance.

2.2 Deposition Approach

2.2.1 Filtration with Following Dry Transfer

The section describes the deposition step of single-walled carbon nanotubes produced by the aerosol CVD technique. The first and the most widespread one is the dry transfer. Since the floating catalyst CVD method was discovered, the samples of SWCNTs were collected by filtering the outlet from the laminar flow reactor using silver filters for carrying out further analysis [57]. In the subsequent experiments, nitrocellulose filters were employed [58]. These filters served a dual purpose: first, they collected carbon nanotubes from their aerosol state, forming a film with a random network structure; and second, this film could be easily detached using tweezers or light pressing and then transferred to a preferred substrate. These ideas were further developed, leading to the widespread adoption of the dry transfer technique (**Fig. 2.1b**).

This technique involves transferring a SWCNT network from a filter onto a flexible polymer substrate at room temperature using a press transfer method. To achieve this, a substrate and the filter with nanotubes are pressed together with a pressure of approximately 10^3 Pa. This pressure ensures a precise and conformal contact between the SWCNT network and the substrate, effectively adhering the network to the substrate. Subsequently, the membrane filter can be easily lifted away [10]. One notable advantage of this technique is its simplicity; it doesn't require any dispersion or cleaning steps before press transfer. As a result, it is significantly faster, cost-effective, and environmentally friendly compared to traditional liquid-based methods for depositing SWCNT networks. The key advantages of this method:

- Easy control of film thickness by simply adjusting the collection time.

- The transfer process itself is remarkably quick, taking only a few seconds.

- It is also possible to customize the shape of the SWCNT-laden filter, allowing for the creation of specific film configurations.

- It can be used to produce freestanding films, adding to its versatility (**Fig. 2.2a**) [66,67].

- This technique applies to a wide range of substrates, including rigid, flexible, and even stretchable materials (**Fig. 2.2b,c**) [68–71].
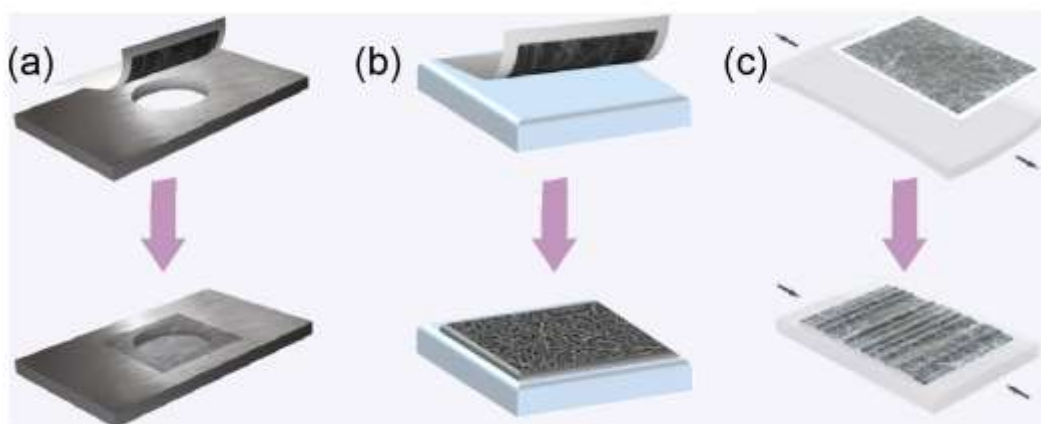
Figure 2.2. Dry transfer of SWCNT thin film onto (a) substrate with hole for producing a freestanding sample, (b) rigid, and (c) stretchable substrate. Image (c) Reproduced with permission [71]. Copyright 2019, American Chemical Society.

However, it's important to point out the limitations of this method. Firstly, the resulting networks are randomly oriented, there is no capability to structure carbon nanotubes in a film. Secondly, it doesn't offer a one-step process for directly depositing

from the aerosol phase onto a substrate. Additionally, it doesn't facilitate the transfer of individual SWCNTs or rarified networks consisting of short nanotubes.

Possible solutions to address these limitations involve incorporating patterning techniques to structure the film and employing alternative deposition methods like thermophoresis and photophoresis for orienting nanotubes within a network and enabling direct deposition.

2.2.2 Thermophoretic Deposition

Thermophoresis refers to the phenomenon in which small particles, such as soot particles or aerosols, suspended in a gas with a temperature gradient, undergo a force that acts in the opposite direction to this gradient (from high- to low-temperature zone) [72]. The underlying physical processes responsible for thermophoresis were initially explored by Maxwell [73]. His investigation aimed to elucidate the radiometer effect. Maxwell demonstrated that when a solid boundary in contact with a gas is heated unevenly, and the mean free path is not significantly smaller than a characteristic dimension of the solid, molecules colliding obliquely with a small area of the boundary impart greater tangential (and also normal) momentum to the wall when originating from the hotter region of the gas, as opposed to the colder region (unless specular reflection occurs). Since then, it has been studied from a scientific point of view and applied industrially in thermal precipitators [72,74].

Recently, thermophoretic deposition attracted attention among scientific groups specializing in aerosol CVD synthesis of carbon nanotubes (**Fig. 2.3**). Laiho *et al.* carried

out studies of SWCNT precipitation using temperature gradient in 2017 [75]. The density of the nanotube film could be altered in a continuous manner, ranging from individual and isolated nanotubes to multilayer thin films, by simply adjusting the deposition time. Since then, this method has been applied to obtain field-effect transistors (FETs) [75,76] and transparent conductors [64,77,78].
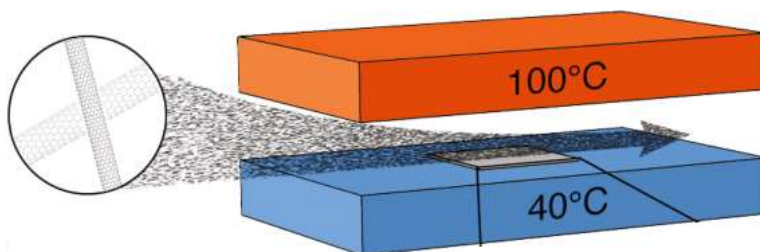

Figure 2.3. Thermophoretic deposition of SWCNTs. Reproduced with permission [75]. Copyright 2017, American Chemical Society.

The key advantages of thermophoresis: this is a one-step technique and it allows convenient deposition of individual SWCNTs directly on a desired substrate. Nevertheless, it does not attribute to any selectivity of the deposition, because the field of temperature gradient affects all the species of nanotubes. These drawbacks can potentially be solved by utilizing the third deposition approach – photophoresis.

2.2.3 Photophoretic Deposition

The nature of the photophoretic phenomenon is similar to thermophoresis, but the temperature gradient here appears by the means of light irradiation. It involves the light-induced movement of particles in either a liquid or gas phase and holds promise as an

unexplored technique for selectively depositing carbon nanotubes [79,80]. According to an explanation by Rubinowitz in 1920 [11], in the case of a highly absorbing particle, the side facing the radiation becomes hotter, leading to photophoresis in the direction of the radiation. Conversely, a particle with low light absorption redirects the light to its rear side, causing it to become hotter, resulting in movement in the opposite direction (**Fig. 2.4**).
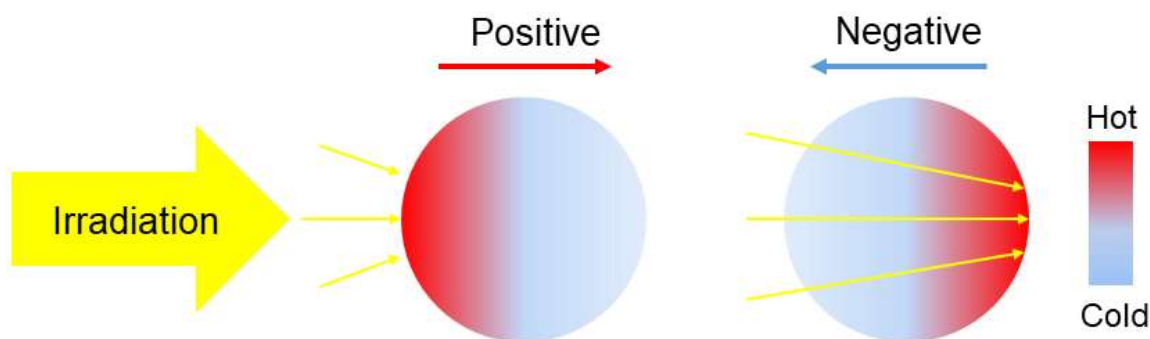
Figure 2.4. The scheme of positive and negative photophoretic motion.

From the point of view of SWCNTs, which we consider highly absorbing particles characterized by positive photophoresis, different chiralities of nanotubes exhibit distinct electronic band structures [81], corresponding to their optical spectra. These variations enable selective excitation at specific wavelengths. When exposed to irradiation at a particular energy level, only a specific fraction of SWCNTs absorbs a defined quantity of photons. This absorption correlates with the velocity of their photophoretic motion. Notably, researchers have previously utilized the photophoretic phenomenon to manipulate various materials in both suspension and aerosol phases. This includes bio-objects in suspension [82,83], polymer particles in aerosol and suspension

[84,85], microparticles of basalt in aerosol [86], metals in suspension [87], metal oxides in suspension [83], micro-droplets of organics in suspension [88,89], and others.

Smith *et al.* conducted calculations that predicted chirality-selective photophoresis in SWCNTs [90]. In their model, the motion in the direction of irradiation propagation is directly related to the energy absorbed by an individual nanotube. However, it's important to note that the theory of photophoresis is still a topic under discussion [91]. While a few pilot experiments have been conducted that demonstrated the motion of large bundles of SWCNTs in a liquid medium induced by irradiation [92,93], the need for nano- and micrometer-scale agglomerates of SWCNTs with clean surfaces and low defectiveness limits liquid-based processing methods. Thus, the approach of depositing carbon nanotubes from the gaseous phase is both novel and highly promising making it an ideal candidate for investigations.

2.3 Doping of SWCNT films

According to Chapter 2.3.1, to improve the optoelectronic properties of SWCNT transparent conductors, post-treatment procedures should be implemented on the films to enhance their conductivity or transparency. Adsorption doping stands out as one of the most potent techniques for enhancing the efficiency of transparent electrodes. This effectiveness arises from the fact that every single atom in SWCNTs resides on their surface. Consequently, any impurity on a SWCNT directly impacts its electronic structure, specifically affecting the concentration of charge carriers and the position of the Fermi level. Additionally, it influences the Schottky barrier between SWCNTs with
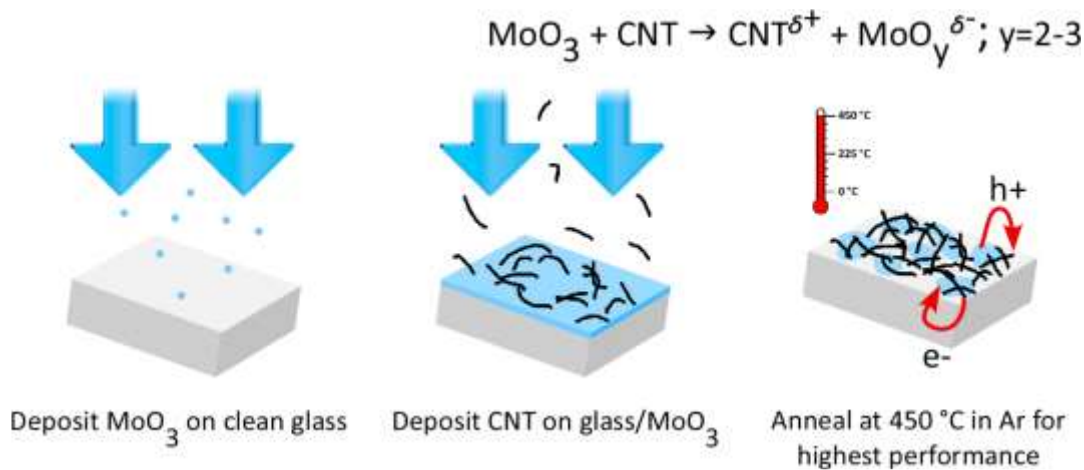
varying chirality/metallicity, a crucial factor that limits the overall conductivity within the nanotube network. Another form of doping, which involves the substitution of carbon with other elements like nitrogen [94–98] or boron [99–103], does indeed alter the electronic structure. However, it comes with a notable downside, as it introduces lattice defects that lead to a significant deterioration in charge transfer properties. Consequently, this alternative approach is not under consideration.

Achieving effective adsorption doping involves balancing between the dopant quantity on the SWCNT surface and the final conductivity and transparency of a film. Typically, a higher doping level leads to enhanced conductivity but at the cost of reduced film transparency. To mitigate this decrease in transparency, control over the uniformity and thickness of the dopant layer can be exercised through various film deposition techniques, such as dip-coating, spin coating, and aerosol deposition. Furthermore, depending on the doping method, solvent evaporation and wettability can also play a key role [63]. The enhancement of optoelectrical performance, characterized by the ratio between initial and resultant equivalent sheet resistances, is contingent upon the quality of the nanotubes. Notably, the most significant improvements are typically observed in lower-quality SWCNT films [1].

Adsorption doping of SWCNTs can be classified into two types: n-type (electron donation) and p-type (electron acceptance). N-type dopants, including metals (Li, K, Cu, Zn, Fe, Co, Ni, Ag, Ti, Zr, Eu, Gd, etc.) [104–107] deposited on or inside SWCNTs, or electron-donating molecules like NADH, viologens, PEI, hydrazine, DMC [108–111], and others applied using simple solution methods. However, n-type-doped SWCNTs

often lack the optoelectronic properties needed for TCFs because SWCNTs tend to become p-doped in ambient conditions due to environmental factors, lowering the Fermi level and reducing electron donation efficiency after n-doping.

The most effective enhancement of carbon nanotube conductivity resulted from p-type dopants like HNO_3 [10,112], $HAuCl_4$ [63,113], and $AuCl_3$ [55,114]. However, these doped SWCNTs exhibit poor time stability due to dopant desorption or decomposition [13,14,115,116]. To solve this issue, stable inorganic compounds with high work functions can be employed for both doping and SWCNT protection. For example, Hellstrom et al. created MoO_3/SWCNT structures via molybdenum oxide thermal evaporation and subsequent carbon nanotube spray coating (**Fig. 2.5**) [117]. These films initially had a sheet resistance of R_{90} = 154 Ω sq^{-1}, which increased to 170 Ω sq^{-1} over 20 days.

$$MoO_3 + CNT \rightarrow CNT^{\delta+} + MoO_y^{\delta-}; \; y=2\text{-}3$$

Deposit MoO_3 on clean glass   Deposit CNT on glass/MoO_3 Anneal at 450 °C in Ar for highest performance

Figure. 2.5. Fabrication of MoO_3/SWCNTs TCF by Hellstrom et al. Reproduced with permission [117]. Copyright 2012, American Chemical Society.

Although MoO_3/SWCNTs may not match the optoelectronic performance of SWCNTs doped by HNO_3 or gold compounds, they exhibit significantly improved stability. Thus, the use of metal oxides for p-type doping of SWCNTs is an important topic for further investigation.

2.4 Rational Design – Combination of Approaches

The concept of rational design of TCFs with improved properties can be approached in two ways: creating composite TCFs that outperform their components or designing specific structures that offer high conductivity and transparency.

For the first time, Zhu *et al.* implemented rational design principles to craft TCFs using a hybrid material combining metallic grids and graphene [118]. This innovation achieved a sheet resistance of 3 Ω sq^{-1} at 80% transmittance (R_{90} = 20 Ω sq^{-1}). Kim *et al.* applied rational design to graphene and carbon nanotubes, resulting in exceptionally transparent composite films [119]. The authors further reduced the equivalent sheet resistance from 104 Ω sq^{-1} by a factor of 3 by introducing $AuCl_3$ as a dopant [120].

Subsequently, various research groups explored the combination of graphene (or reduced graphene oxide) and SWCNTs [121–123]. Zhu *et al.* introduced a method to create a three-layer film based on SWCNTs modified with tannic acid, Ag nanowires, and PEDOT:PSS, resulting in exceptional optoelectrical properties with R_{90} = 16 Ω sq^{-1} [124]. Similarly, Rajanna et al. achieved R_{90} = 17 Ω sq^{-1} for SWCNT-based TCFs, successfully implementing them in a-Si solar cells [113]. This rational design involved coating SWCNTs with MoO_3 (a dopant with a high work function), subsequent doping

28

with $HAuCl_4$, and PEDOT:PSS deposition. Lastly, SWCNT fibers, obtained through the wet pulling method, were deposited as current collectors to enhance electrode conductivity. Consequently, this rational design is a combinative approach that applies various techniques: doping, patterning, and the development of complex multilayer hybrid materials based on carbon nanotubes, and is the main trend for obtaining the best performance for SWCNT-based TCFs.

To reach the aim of rational design development, the following objectives were formulated:

1. To develop a method for selective deposition of nanotube aerosol based on photophoretic phenomenon.

2. To develop a robust technique for stable and effective doping through the deposition of a V_2O_5 (material with high work function) coating layer.

3. To calculate the fundamental limits of SWCNT-based transparent conductive films by elaborating its ideal network with the highest optoelectronic performance.

3. Methods

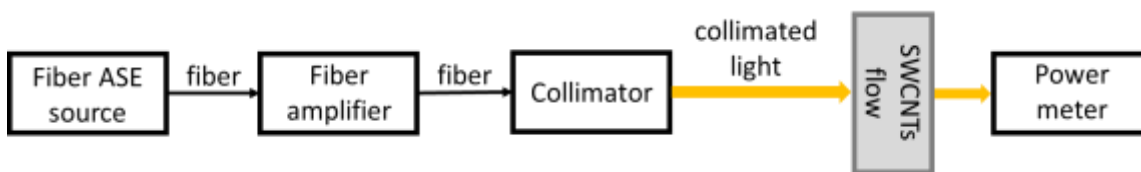### 3.1 Photophoretic Deposition of SWCNTs

In this study, we synthesized high-quality single-walled carbon nanotubes (SWCNTs) using the aerosol (floating catalyst) CVD technique, employing a CO-based reactor as previously described. At the reactor outlet, we generated an aerosol of single-walled carbon nanotubes with an average concentration of 3×10^5 particles/cm3 and an effective mean size of 103 nm when irradiated with LED light (ARPL-200W-BCB-7080-PW, 7000 mA), and with an average concentration of 2×10^3 particles/cm^3 and a mean size of 70 nm when irradiated with a 1550 nm laser.

Subsequently, the aerosol SWCNT flow was directed into a photophoretic cell, as illustrated in **Figure 3.1**. Within the cell, SWCNTs were deposited onto a 5 mm quartz substrate under the influence of photophoretic forces, while the remaining nanotubes were collected downstream on a nitrocellulose membrane filter (HAWP, Merck Millipore, USA). These collected SWCNTs were then subject to dry transfer onto a quartz substrate for further analysis. The samples were collected for different times: 15, 30, 45, and 60 minutes; 3 times at each time. The photophoretic cell featured a transparent window with a slot for accommodating the substrate, and the aerosol velocity, determining the residence time for irradiation, was controlled using a vacuum system that included a valve, flowmeter, and vacuum pump with a nozzle valve.
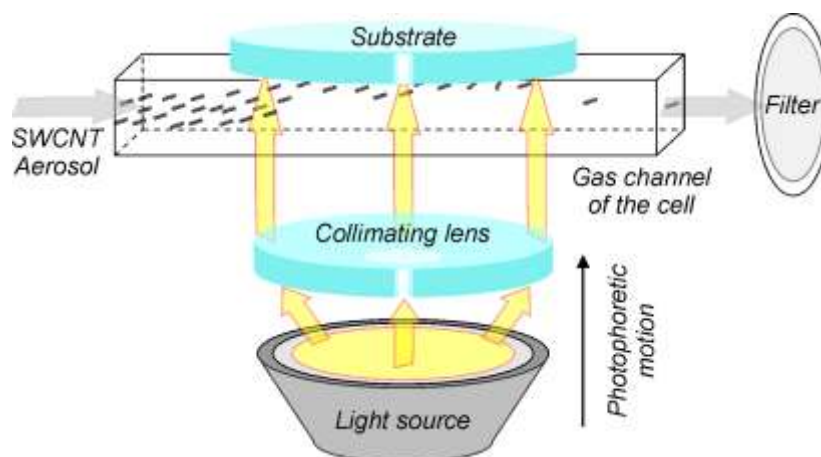
Figure 3.1. Scheme of the setup for photophoretic deposition of SWCNTs.

For SWCNT deposition, we employed two different light sources: a white-light LED lamp and a fiber-amplified spontaneous emission (ASE) source equipped with a collimating lens. The experimental setup for deposition using the fiber ASE source is depicted in **Figure 3.2**. In the latter case, we utilized an erbium-doped fiber ASE source, and the emitted light was amplified by a commercial erbium-doped fiber amplifier (Keopsys PEFA-SP-C-PM-27-B130-FA-FA), resulting in an emission spectrum spanning from 1520 to 1620 nm. A Thorlabs F810APC-1550 collimator was employed to couple the light from the fiber into free space, and the light power was monitored using a Thorlabs PM100D power meter. The diameter of the light beam for both setups was 5 mm, with the LED and ASE sources with the measured power of 6.0 W and 0.6 W, respectively. We meticulously ensured that the photophoretic cell's windows were transparent to the working wavelengths and that the spectral characteristics of the light sources remained stable.

Figure 3.2. Scheme of the experimental setup for the photophoretic deposition of SWCNTs using the amplified spontaneous emission source.

3.2 Doping of SWCNTs by V_2O_5

SWCNTs were produced *via* aerosol-based chemical vapor deposition, employing ferrocene as a catalyst precursor, toluene and C_2H_4 as hybrid carbon sources, and thiophene as a sulfur-based promoter [125], as previously detailed elsewhere [126,127]. The resulting SWCNTs were gathered at the exit of the reactor, forming a thin film of randomly oriented nanotubes on a nitrocellulose membrane filter (HAWP, Merck Millipore, USA). Subsequently, these films were transferred to either quartz substrates using the dry transfer technique. The dimensions of the samples were standardized at 10 × 10 mm^2, offering 90% transmittance at 550 nm.

A V_2O_5 layer was obtained on the surface of SWCNTs through hydrolysis and polycondensation reactions under ambient conditions, employing vanadyl triisopropoxide (VTIP) (98%, Sigma-Aldrich) as the precursor, as depicted in **Fig. 3.3.** The precursor was diluted in isopropanol (99.5%, Sigma-Aldrich) at various volume ratios (ranging from 1:75 to 1:1000) within a nitrogen atmosphere. Subsequently, the mixture was spin-coated onto the SWCNT film using an Ossila L2001A3-E461-EU spin coater at 4000 rpm for 60 seconds under ambient conditions.
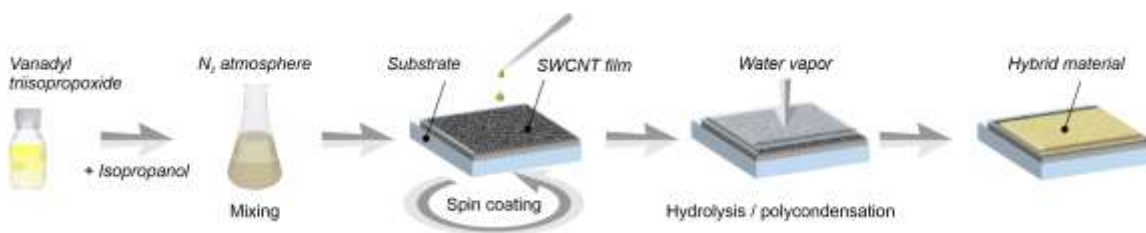
Figure 3.3. Scheme of SWCNT coating at ambient conditions by nanometer-thick V_2O_5 layer using vanadyl triisopropoxide (VTIP) dissolved in isopropanol. Reproduced with permission [12]. Copyright 2023, The Royal Society of Chemistry.

3.3 Characterization

The optical transmittance spectra of SWCNT films were obtained using a PerkinElmer LAMBDA 1050 UV-Vis-NIR spectrophotometer. Raman spectra of the films were collected using the Horiba LabRAM HR Evolution Raman Spectrometer, equipped with a laser with wavelengths of 633 nm (HeNe, 17 mW). Each Raman measurement was carried out for 3 samples, while 5 measurements were taken 8 for each of them, with an exposure time of 60 seconds and an accumulation time of 10 seconds, and then averaged. The topography of the quartz substrate with deposited SWCNTs and nanoparticles was examined using a Bruker Multimode V8 Atomic Force Microscope (AFM) in Peak-Force™ mode. Each substrate was characterized 10 times at different positions to determine the average concentration of deposited object intensity per square unit. The spectrum of the LED lamp (ARPL-200W-BCB-7080-PW, 7000 mA) was measured by Ocean Optics QE Pro spectrometer.

For photoluminescence detection, a tunable laser light source (C-WAVE, HÜBNER Photonics) and a spectrometer (iHR320, Horiba) with multiple gratings were

employed, including a 600 grooves/mm grating with a blaze at 750 nm and a 150 grooves/mm grating with a 1200 nm blaze. Detection was carried out with a linear multi-pixel InGaAs liquid-nitrogen-cooled array (Symphony II, Horiba) known for its high quantum efficiency from 1000 to 1600 nm. The objective used was a 100x NIR (Mitutoyo Plan Apo NA=0.7) with a focal spot radius of approximately 0.8 μm.

The sheet resistance of the samples was determined using the linear four-probe method, utilizing the Jandel RM3000 Test Unit. To investigate the morphology of the films, transmission electron microscopy (TEM) was employed, with a FEI Tecnai G2 F20 instrument. X-ray diffraction (XRD) data were gathered using the Bruker D8 Advance diffractometer, using CuKα radiation. In-situ synchrotron radiation XRD measurements were conducted at the Siberian Synchrotron and Terahertz Radiation Centre at the Budker Institute of Nuclear Physics. The V_2O_5/SWCNT samples were heated using the XRK-900 reactor chamber (Anton Paar, Austria), equipped with a fast, parallax-free one-coordinate X-ray detector OD-3M, and a mass spectrometer (UGA 100, Stanford Research Systems, USA). Reflex positions were calibrated using a standard sample (SRM676) at a wavelength of 0.1732 nm.

Climatic tests were performed in the KHTV-0.03 chamber (Russia) under two conditions: in mild conditions at 25°C and 40% relative humidity (RH), and in the damp heat steady state at 35°C and 100% RH, as well as at 60°C and 100% RH, following the standard IEC 60068-2-78.

Kelvin Probe Force Microscopy measurements were carried out in a 2-pass amplitude modulation mode using a Pt-coated Si cantilever with a Cypher ES atomic

force microscope from Asylum Research (Oxford Instruments), installed in an Ar-filled glove box (MBraun). The second pass height was set at 50 nm, and the cantilever was calibrated using ZYA-grade highly oriented pyrolytic graphite (HOPG).

Elemental analysis was conducted by X-ray photoelectron spectroscopy (XPS) using a Kratos Axis Ultra spectrometer with monochromated Al Kα radiation, charge neutralization, a pass energy of 20 eV, X-ray power of 195 W, and an analysis area of approximately 700 µm × 300 µm. The binding energy scale was referenced to the C 1s peak of SWCNTs at 284.4 eV. The measurement time was limited to a few minutes due to the observed photoreduction of V^{5+} to V^{4+}. Peak fitting in the V 2p region was performed using CasaXPS software after Shirley background subtraction. Properly fitting the V 2p region involved extending the background over the O 1s peak, which was also fitted. Gaussian-Lorentzian peaks with a V 2p1/2–V 2p3/2 splitting of 7.35 eV and a V 2p1/2/V 2p3/2 area ratio of 0.5 were used, and peak positions and full widths at half-maximum were allowed to vary within reported limits.

4. Results and Discussion

4.1 Photophoretic Deposition of SWCNTs

4.1.1 Calculations for Cell Construction

The photophoresis phenomenon is fundamentally reliant on the interaction between dispersed particles and their surrounding medium. To establish boundary conditions for different flow regimes, the Knudsen number (Kn) is a crucial parameter. Kn compares the characteristic size of particles to the mean free path of medium molecules and is defined as follows:

$$Kn = \frac{2l}{d}, \qquad (4.1)$$

where l represents the mean free path of gas molecules, and d denotes the particle diameter [128]. In the case of $Kn > 10$, referred to as the free molecular regime, the particle diameter is significantly smaller than the mean free path, and gas-kinetic theory is employed for modeling. Conversely, when $Kn < 10^{-3}$, known as the continuum regime, the mean free path is much smaller than the particle diameter, and continuum mechanics are used for calculations [91].

In 1920, Rubinowicz defined the photophoretic force (F) acting on spherical particles in a gaseous medium in the free molecular regime as follows [11,80]:

$$F_{free} = \frac{\pi}{12} \cdot \frac{\alpha \cdot d^3 \cdot p}{T} \cdot \mathrm{grad}T, \qquad (4.2)$$

where α is the accommodation coefficient [128], p is the pressure of the surrounding gas, T is the gas temperature, and $\mathrm{grad}T$ is the value caused by temperature change on a particle surface:

$$gradT = \frac{\Phi}{2(k_p + k)}, \tag{4.3}$$

where Φ is the flux density of the illumination (i.e., irradiation intensity), k_p is the thermal conductivity of the particle, and k is the thermal conductivity of the surrounding gas. For the continuum regime, which considers thermal creep and resulting viscous forces around the particle, Hettner defined the photophoretic force in 1926 as [129]:

$$F_{cont} = \frac{3\pi}{2} \cdot \frac{\eta^2 \cdot d \cdot R}{p \cdot M} \cdot gradT, \tag{4.4}$$

where η is the viscosity of the gas, R is the gas constant, and M is the molecular weight of gas molecules. The key parameters for defining photophoretic force are the particle size, illumination flux density, and the thermal conductivity of both particles and the medium, all of which are correlated with the nature of the photophoresis phenomenon.

Subsequent research aimed to provide more accurate definitions of $gradT$, considering the behavior of nanoparticles in the aerosol phase. In 1995, Rohastek summarized existing theories and derived semi-empirical models for the free molecular (Eq. 4.5) and continuum (Eq. 4.6) regimes [130]:

$$F_{free} = \frac{\alpha \cdot D \cdot J_1}{4 k_p} \cdot \frac{p}{p^*} \cdot d^2 \cdot \Phi, \tag{4.5}$$

$$F_{cont} = \frac{D \cdot J_1}{2 k_p} \cdot \frac{p^*}{p} \cdot d^2 \cdot \Phi, \tag{4.6}$$

where D is a constant determined by the gas state (Eq. 4.7), p^* is the reference pressure (dependent on particle radius, Eq. 4.8) [130], and J_1 is a photophoretic asymmetry factor of a particle [131].

$$D = \frac{\pi}{2} \sqrt{\frac{\pi}{3}} \kappa \sqrt{\frac{8RT}{\pi M}} \cdot \frac{\eta}{T}, \tag{4.7}$$

$$p^* = \frac{6}{\pi} \cdot D \cdot \frac{T}{d},$$ (4.8)

where κ is the thermal creep coefficient.

To calculate the photophoretic velocity and process efficiency for SWCNT deposition, we considered two approaches. First, we assessed the velocity for a spherical particle in the transition regime ($10^{-1} < Kn < 10$) with an effective diameter of $a = 103 \, nm$. Based on the photophoretic force, the photophoretic velocity of a spherical particle U_{sp} can be calculated according to Mackowski (1988) [132]:

$$U_{sp} = -\frac{2C_s J_1 \eta I}{3k_p \rho T_\infty} \cdot \frac{1 + 2l/a(1.2 + 0.41e^{-0.88a/2l})}{(1 + 3C_m^*)(1 + 2C_t^* + 2k/k_p)},$$ (4.9)

where

$$C_m^* = 2C_m l/a,$$ (4.10)

$$C_t^* = 2C_t l/a,$$ (4.11)

$$I = P/S.$$ (4.12)

C_s is the thermal slip coefficient, C_m is the frictional slip coefficient, C_t is the temperature jump coefficient [72], C_m^* and C_t^* are dimensionless parameters defined by Eqs. (4.10) and (4.11), respectively. I is the intensity of irradiation, P is the power of an irradiation lamp, S is the irradiation spot area, ρ is the density of CO at 298 K, T_∞ is the gas temperature.

As the 2nd method for determining photophoretic velocity, we examined a bundle of SWCNTs, treating it as a cylindrical particle. Based on AFM measurements, the average diameter of the SWCNT bundle $a = 19 \, nm$, aligns it with the transition regime. The model for cylindrical particles operating within a continuum regime was originally

outlined by Keh and Tu in 2002 [133] and later expanded to encompass smaller particles in 2017 [134]:

$$U_{cyl} = -\frac{(C_s + 2C_h C_m^*)J_1}{2(1 + 2C_m^*)(1 + k^* + k^* C_t^*)} \cdot \frac{\eta I}{k\rho T_\infty},$$ (4.13)

where

$$k^* = k_p/k,$$ (4.14)

U_{cyl} is the photophoretic velocity of a cylindrical particle, k^* is the ratio of thermal conductivities between a particle and CO, C_h is the thermal stress slip coefficient. Since SWCNTs exhibit light-absorbing properties, we attribute a negative sign to J_1 value. Consequently, velocity should exhibit a positive value, indicating an anticipated co-directional photophoretic movement aligned with the vector of light propagation (positive photophoresis). SWCNTs of varying chiralities may exhibit distinct values for this parameter. For our modeling purposes, we adopt a conservative approach by using the limit value for J_1 = -0.5, which yields the highest velocity. To calculate the efficiency of the deposition according to both types of particles, we considered the following model:

$$\frac{dN}{N} = -\frac{U}{h} dt,$$ (4.15)

where N is the total number of particles, dN/N is the fraction of deposited particles, U is the photophoretic velocity of a spherical or cylindrical particle calculated according to Eq. 4.9 and 4.13, respectively, dt is the residence time of particles in the cell under irradiation, h is the thickness of the cross-section of the gas channel in the cell. Eq. 15 is to be integrated over limits N_{out} and N_{in}, which are respectively the total numbers of particles at the outlet and inlet of the photophoretic cell:

$$\int_{N_{in}}^{N_{out}} \frac{dN}{N} = \int_0^t \left(-\frac{U}{h} dt\right), \tag{4.16}$$

$$\frac{N_{out}}{N_{in}} = \exp\left(-\frac{U}{h} t\right). \tag{4.17}$$

Thus, the efficiency of photophoretic deposition E can be defined as:

$$E(\%) = 1 - \frac{N_{out}}{N_{in}} = \left(1 - \exp\left(-\frac{U}{h} t\right)\right) \cdot 100\% \tag{4.18}$$

To enhance deposition efficiency and prevent the formation of additional vortexes within the aerosol flow through the cell, we established a fixed thickness for the aerosol channel, set at $h = 1$ mm. During the modeling of the photophoretic cell, we conducted variations in two crucial parameters: the power of the light source, denoted as P, and the residence time within the cell, represented as t. The resulting deposition efficiencies, as calculated using Eq. 4.18 for both spherical and cylindrical particles, are depicted in **Figure 4.1**.

The highest deposition efficiency naturally occurs when we maximize both the residence time and the irradiation power. In our experimental setup, we utilized a commercially available LED source compatible with laboratory settings, delivering a power output of 6.0 W. To achieve a residence time of 0.3 seconds, we maintained a flow rate of 5 cm³/min through the photophoretic cell, designed with specific dimensions: a rectangular deposition channel measuring 1 x 5 mm² and having a thickness of 1 mm. Remarkably, the efficiency values remain nearly identical for both spherical and cylindrical model objects, standing at 5.3% and 4.2%, respectively. These results are sufficiently robust for validating the proof of concept.
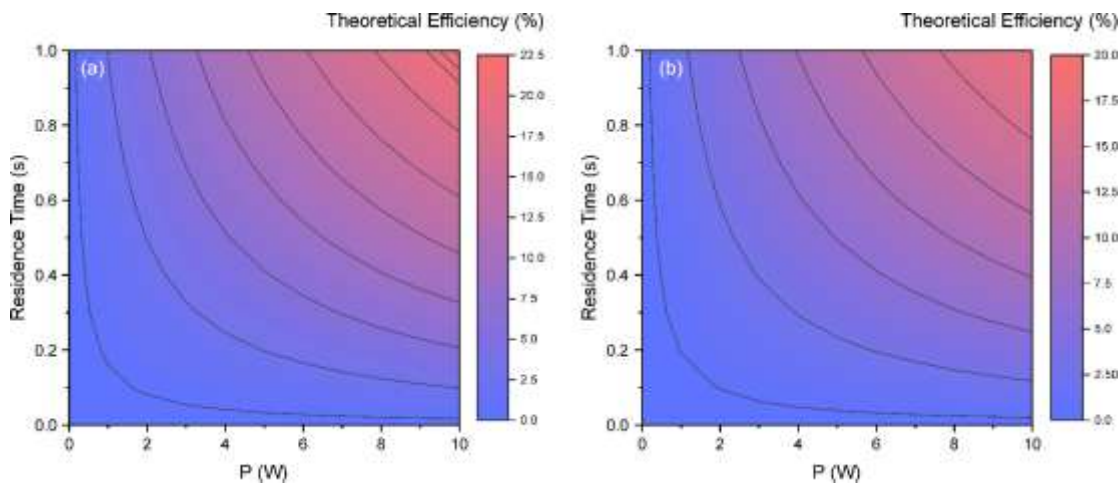
Figure 4.1. The efficiency of photophoretic deposition as a function of the SWCNT residence time in the cell and the irradiation source power for (a) spherical (Eq. 4.9) and (b) cylindrical (Eq. 4.13) particles.
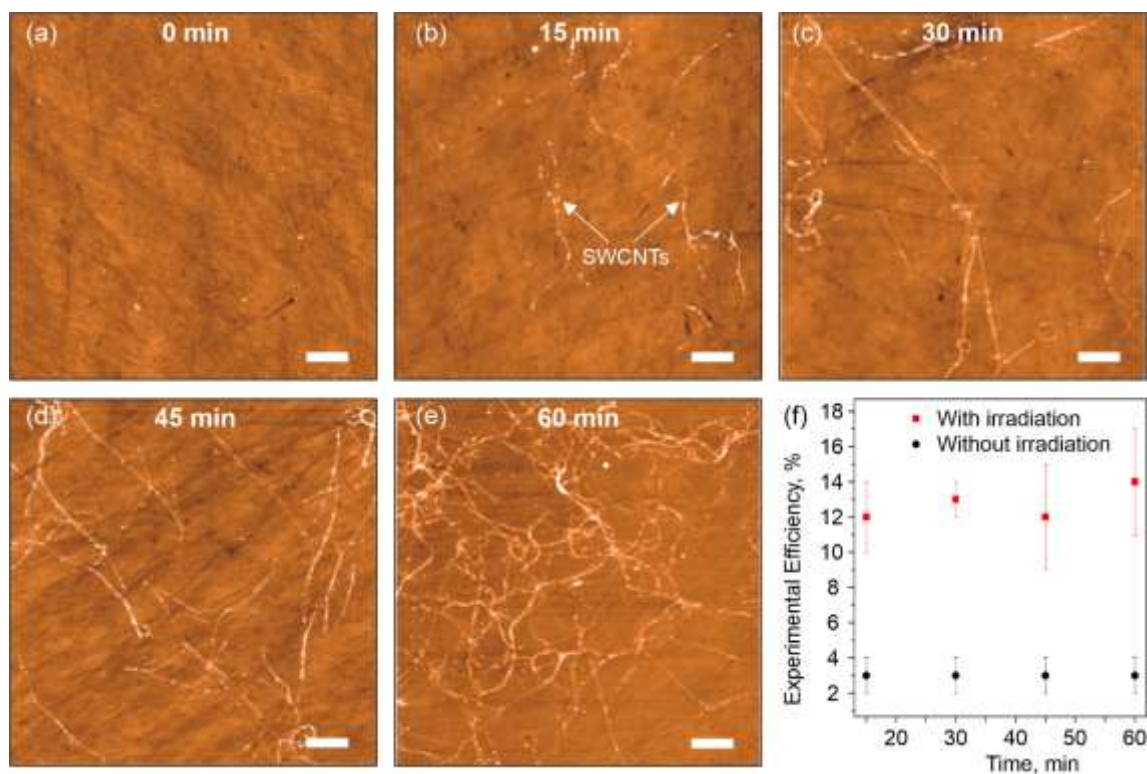
4.1.2 Photophoretic Deposition

We conducted experiments to evaluate the deposition of nanotubes on quartz substrates using AFM. We collected samples over varying time intervals: 15, 30, 45, and 60 minutes, both with and without light irradiation. Each collection time was repeated in 10 separate experiments. The typical topography of the samples obtained after irradiation is illustrated in **Fig. 4.2a-e**. We observed a gradual transformation of deposited bundles, evolving from individual and sparsely bundled species (at 15 minutes) to intricate, branched structures and networks (between 30 and 60 minutes). To ensure the data's representativeness, we computed the average number of precipitated bundles per 100 μm^2 of substrate area. The experimental deposition efficiency, denoted as E_{exp}, is calculated

as the ratio of the number of particles deposited on the substrate, N_{dep}, to the number of particles introduced into the photophoretic cell, N_{in}:

$$E_{exp} = \frac{N_{dep}}{N_{in}} \cdot 100\%. \tag{4.19}$$

The results of the efficiency measurements are presented in **Figure 4.2f**. It is important to mention that, apart from the photophoresis phenomenon, the SWCNT aerosol is also subject to Brownian diffusion, which can potentially influence the results. Since diffusion operates in both directions concerning photophoresis, its impact on efficiency is relatively minor. To assess the contribution of the diffusion process, we conducted deposition efficiency measurements under identical conditions but without laser irradiation. Our findings indicated that deposition due to Brownian diffusion accounted for approximately 3%.

In summary, we have successfully achieved the photophoretic deposition of SWCNTs from an aerosol phase using an LED lamp, resulting in an efficiency of approximately $10 \pm 2\%$ (based on 10 samples). This result aligns well with theoretically calculated values.

Figure 4.2. AFM images of the quartz substrate after (a) 0, (b) 15, (c) 30, (d) 45, (e) 60 minutes of exposure in the photophoretic cell with LED irradiation (scale bar = 1 μm); (f) the efficiency of SWCNT deposition taking into account standard deviation in the photophoretic cell caused by diffusion (black dots) and by diffusion + photophoresis (red dots).

4.1.3 Characterization of LED-Deposited SWCNTs

To assess the impact of light exposure on SWCNT properties, we conducted Raman measurements (**Fig. 4.3**). In the absence of irradiation, reference samples deposited on a substrate and those collected on a filter exhibited nearly identical ratios of Raman intensities for the G and D modes ($I_G/I_D \approx 20$). However, when subjected to LED

irradiation, a redistribution of peak intensity occurred: the I_G/I_D ratio decreased for SWCNTs deposited on a photophoretic substrate but increased for SWCNTs collected by a filter.

Inactive catalyst nanoparticles present in the aerosol flow may experience strong photophoretic motion, leading to their deposition on the substrate. These particles may contain defective carbon shells with a high intensity of the D mode [135]. Consequently, their presence reduces the I_G/I_D ratio for deposited SWCNTs while increasing it for the fraction that remains unprecipitated. Therefore, the irradiation process can be regarded as a cleansing procedure for SWCNTs collected on a filter, a topic warranting further investigation in future studies.
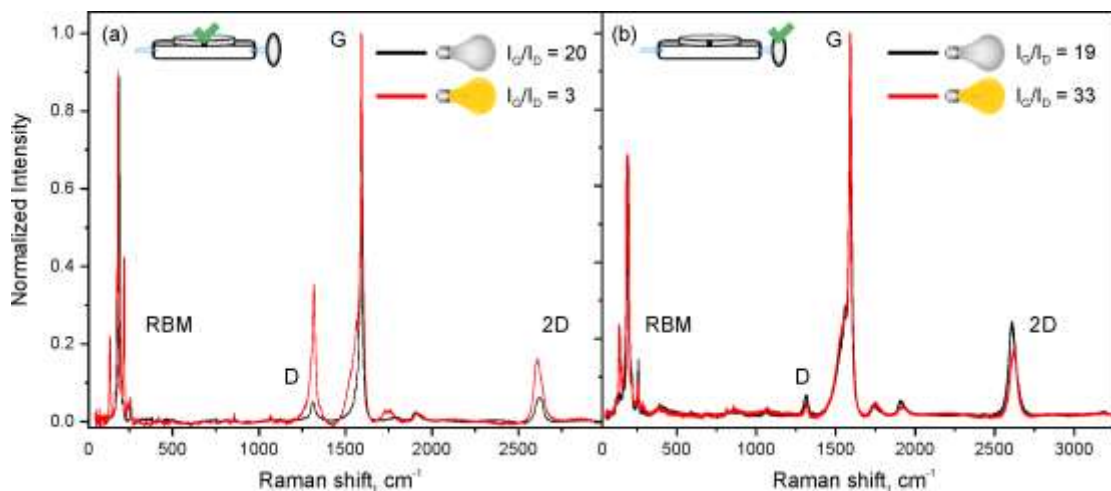
Figure 4.3. Raman spectra of SWCNT samples deposited on a substrate (a) and of an unprecipitated fraction (b) with (red line) and without (black line) LED irradiation. 633 nm – wavelength of excitation laser.

In **Figure 4.4**, we illustrate the radial breathing modes (RBM) found in Raman spectra (averaged from 5 spectra) for carbon nanotubes deposited on a substrate under LED irradiation and in the absence of it. This depiction highlights a noticeable rearrangement in peak intensity, providing evidence for the chiral selectivity of deposition through light irradiation.
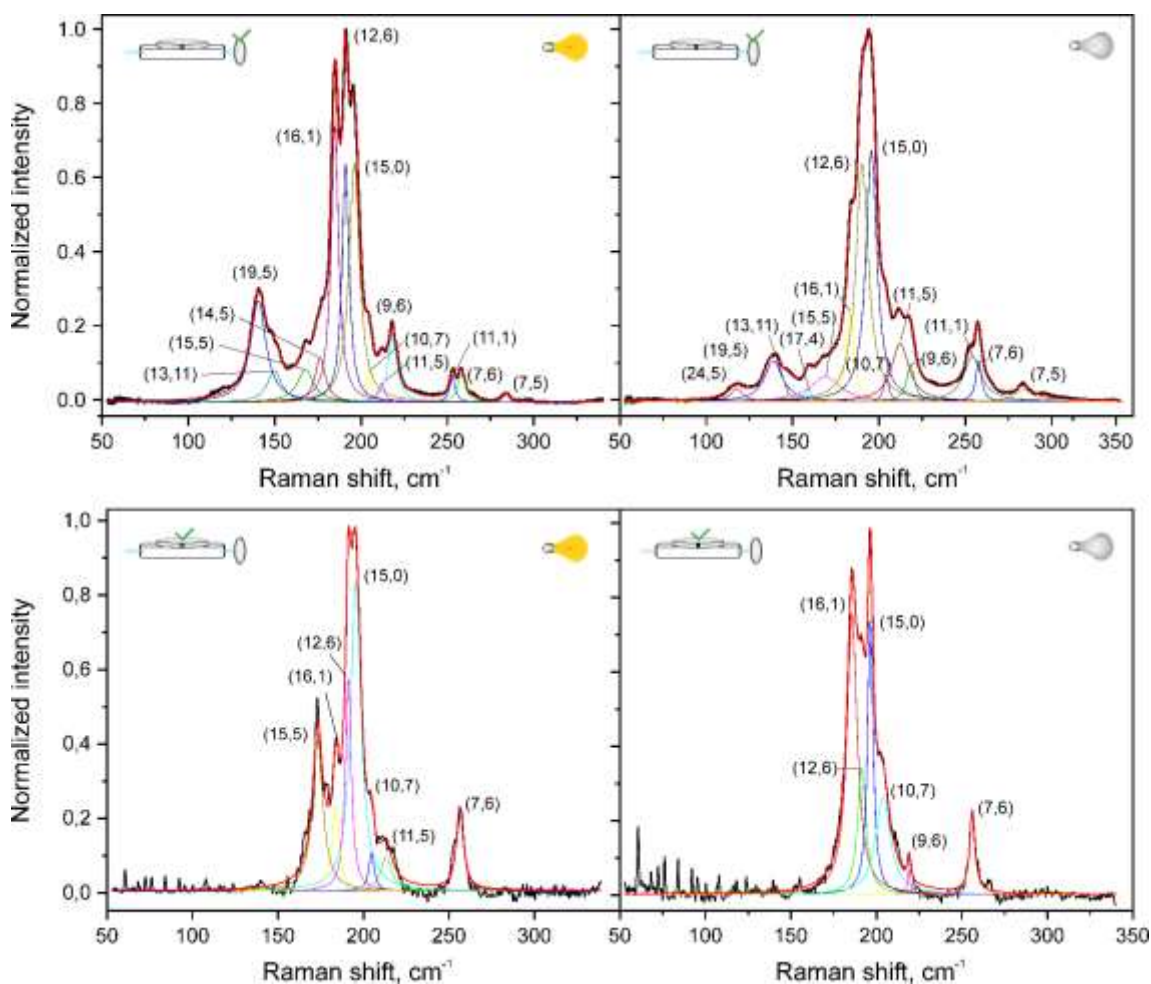
Figure 4.4. Deconvolution of Raman RBM region spectra of SWCNT into Gaussian components of different chiralities. 633 nm – wavelength of excitation laser.

The RBM spectra of samples obtained directly from the reactor outlet align with those collected at the photophoretic cell outlet without irradiation. Consequently, we can treat spectra collected without irradiation as the initial ones. Examining a representative spectrum, notable redistributions that surpass measurement fluctuations include an increase in the percentage of (15,5) chirality from 0% to 17% and (12,6) from 14% to 23%. The chiralities derived from the initial spectrum (Fig. 4.4, bottom right) characterize the specific SWCNT synthesis conditions.

In a simplified form, the photophoretic asymmetry factor for a spherical particle can be expressed as follows [132]:

$$J_1 = 4\pi n\kappa \frac{\alpha}{\lambda} \left(\frac{3(n-1)}{8n^2} - \frac{4}{5}\pi n\kappa\alpha \right), \tag{4.20}$$

where n and κ are real and imaginary parts of complex refractive index, λ is the wavelength of irradiation. The photophoretic asymmetry factor depends on real and imaginary parts of complex refractive index [134], a characteristic that varies among different chiralities of SWCNTs [136]. Consequently, we propose that SWCNTs change their mobility, leading to the observed redistribution of relative intensity outlined in **Table 1**. The percentages presented in Table 1 are accurate for SWCNTs in resonance with the 633 nm laser.

In the context of positive photophoresis, J_1 can range from 0 (indicating no motion) to -0.5 (indicating the highest velocity), resulting in varying photophoretic velocities (equations 4.9 and 4.13) and, consequently, different deposition efficiencies. Therefore, SWCNTs with distinct chiralities exhibit diverse deposition efficiencies at specific irradiation wavelengths, facilitating selective deposition. Moreover, employing a

narrow spectrum of irradiation alongside SWCNT aerosols with elevated concentrations of individual species may lead to the saturation of SWCNT deposition with a specific band structure. This saturation aligns with the wavelength of the irradiation spectrum. Subsequent exploration in the following chapter checks this hypothesis.

Table 1. Estimation of the Raman intensity of SWCNTs with different chiralities (deposited on a quartz substrate) was carried out based on the data shown in **Fig. 4.4**.

Chirality	Relative Intensity (LED off), %	Relative Intensity (LED on), %
(7,6)	10	9
(9,6)	3	0
(11,5)	0	4
(10,7)	11	4
(15,0)	30	34
(12,6)	14	23
(16,1)	32	9
(15,5)	0	17

### 4.1.4 Characterization of Laser-Deposited SWCNTs

As photophoretic deposition by LED indicated partial selectivity, we have replaced the light source with the 1550 nm fiber ASE source (**Fig. 3.2**) to address energy to fewer chiralities of SWCNTs. We also adjusted the synthesis conditions to produce individual aerosol SWCNTs and at the same time to have the S_{11} peak coinciding with the laser

wavelength of 1550 nm [8].

Raman spectroscopy at a fixed excitation wavelength also in the case of very sparse networks of carbon nanotubes cannot serve as an accurate method for the analysis of chirality. For that purpose, we utilized photoluminescence spectroscopy, which was used to examine the samples deposited by the 1550 nm laser irradiation [137,138]. To achieve a representative data set in a wide range of nanotube diameters, we chose 3 wavelengths for the PL excitation: 910, 595, and 467 nm (**Fig. 4.5**).

Fig. 4.6 shows the absorbance spectra of pristine SWCNTs without light irradiation to demonstrate their intersection with the spectra of light sources. According to **Fig. 4.6b**, initial SWCNTs used for the laser deposition demonstrated rather broad diameter distributions with optical absorption peaks that partially overlap with the laser wavelength at 1550 nm. To increase the representativeness of the data set we used not only the excitation at around E_{22s} transition (910 nm) of tubes that should emit at around 1550 nm (but also wavelengths (467 nm and 595 nm) that initially should be resonant to excitation of the majority of tubes with other types of diameters.

Emission distributions (detailed in **Fig. 4.7**) for all excitation wavelengths exhibit saturation in the 1500-1600 nm range, aligning with the irradiation laser spectrum. This is likely attributed to the deposition of SWCNTs with absorbance peaks from **Table 2**.
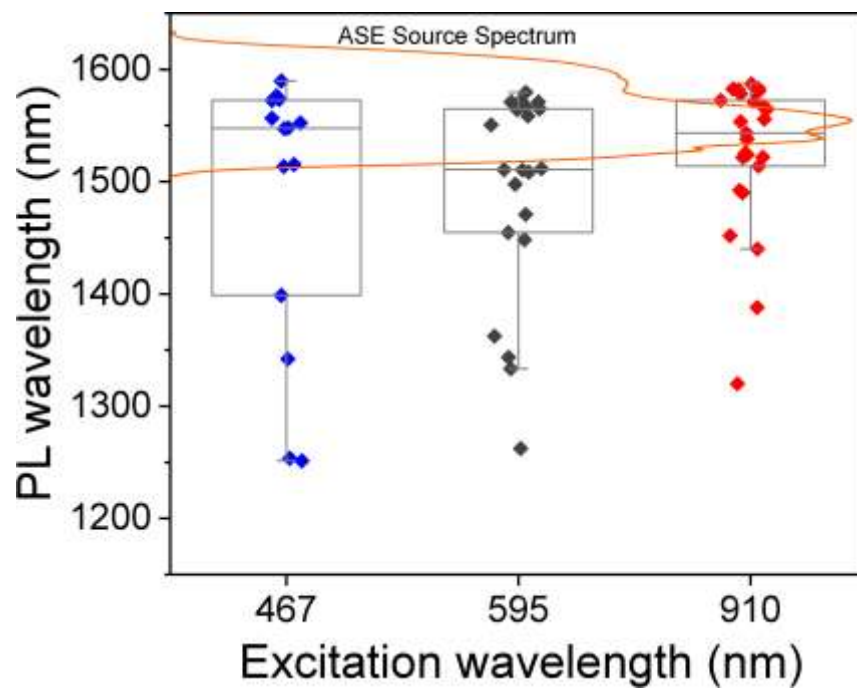
**Figure 4.5.** Statistics of the PL peak maxima obtained at 20 different spots of the SWCNT sample deposited by the broadband laser (1550 nm) under excitation at 910, 595, and 467 nm wavelengths. The orange line is the spectrum of the ASE source.
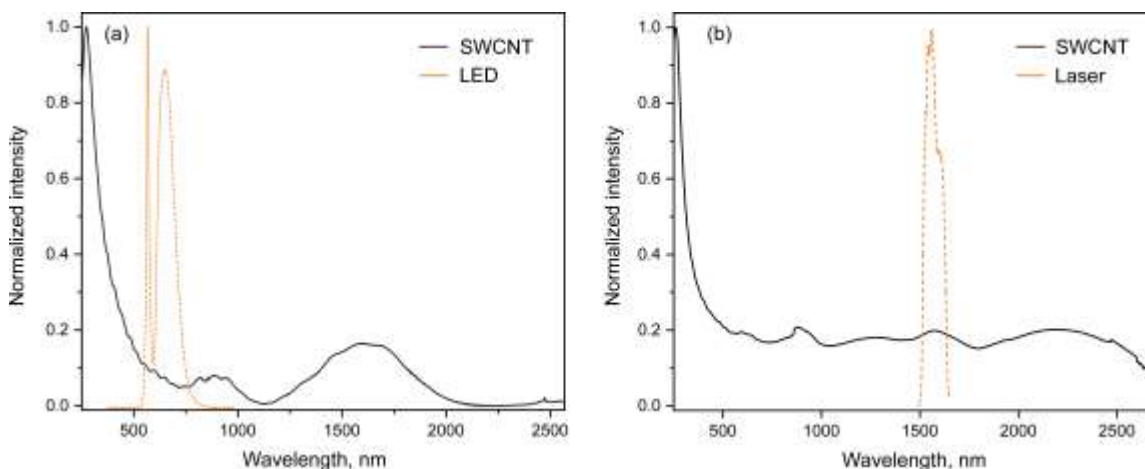
Figure 4.6. UV-vis-NIR absorbance spectra of SWCNTs and spectra of light emitted by LED (a) and ASE (b) sources used for the photophoretic deposition.

Indeed, the statistics of the PL peak maxima at 1550 nm variate slightly depending on the excitation wavelength, which can be explained by the fact that the initial distribution of the SWCNTs in the reactor should result in different values for the PL peak maxima depending on the excitation wavelength. For 467 nm and 595 nm wavelengths, the excitation does not specifically match the S_{22} transition, nevertheless, for all of the excitation wavelengths used, we detect the dominant PL emission around 1550 nm, proving that laser radiation resulted in the selectivity of the deposition. We assume that the presence of PL peaks outside of the irradiation region may indicate the deposition of SWCNT due to the Brownian diffusion.

Thus, these results open a new avenue for direct chiral deposition of carbon nanotubes from an aerosol flow by light irradiation. For example, it may be useful for the fabrication of field effect transistors from SWCNTs with a specified band gap [139,140], optical sensors [141,142], and single-photon sources [143,144].
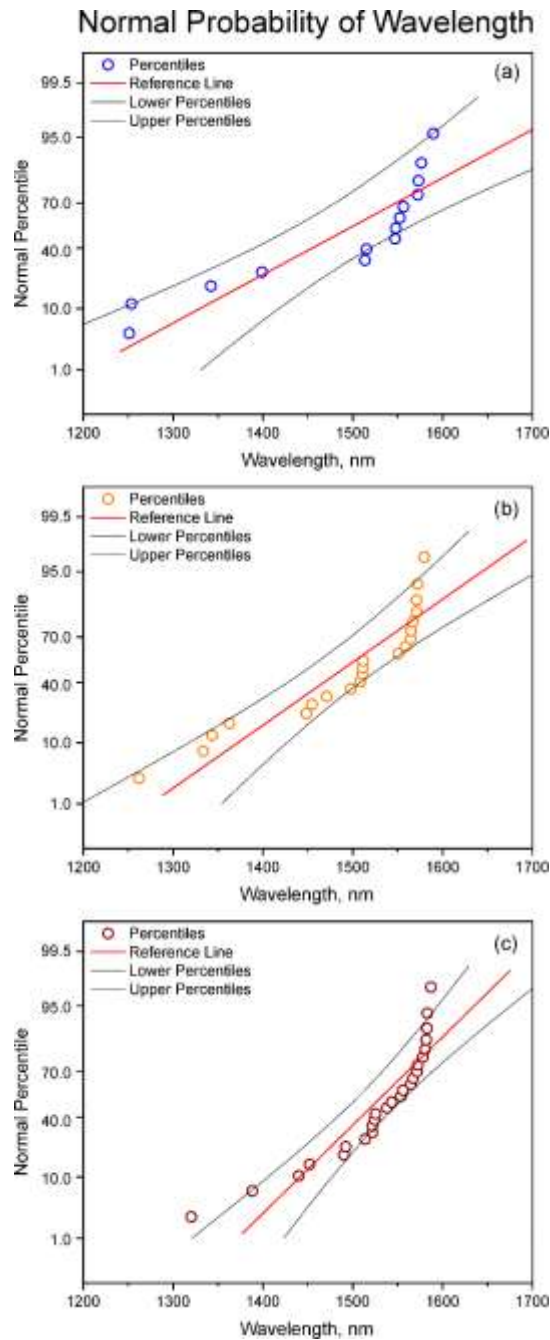
Figure 4.7. Normal probability plots of PL distribution of the samples, deposited by 1550 nm laser and excited by (a) 467, (b) 595, and (c) 910 nm lasers. Lower and upper percentiles show the spread in the normal distribution according to the equation $x = \mu \pm Z \cdot \sigma$, where μ is the mean value, σ is the standard deviation, and Z is the standard score.

Table 2. Chirality of SWCNTs with S_{11}/S_{22} peaks in the range 1500 – 1600 nm.

n	M	S_{11}, eV	S_{22}, eV	λ(S_{11}), nm	λ(S_{22}), nm
14	1	0.813	1.625	1525	763
13	3	0.816	1.595	1520	777
12	5	0.809	1.544	1532	803
10	8	0.820	1.450	1512	855
11	7	0.794	1.479	1561	838
13	5	0.811	1.369	1529	905
12	7	0.782	1.350	1586	919
17	0	0.787	1.273	1575	974
16	2	0.777	1.278	1595	970
29	0	0.483	0.818	2566	1516
28	2	0.479	0.821	2587	1510
27	4	0.474	0.819	2616	1514
26	6	0.467	0.816	2654	1519
21	13	0.461	0.814	2691	1523
25	8	0.461	0.807	2688	1536
24	10	0.454	0.798	2733	1554
18	17	0.443	0.810	2799	1530
20	15	0.449	0.800	2764	1550
25	9	0.437	0.819	2836	1514
21	14	0.438	0.815	2833	1522
30	1	0.462	0.782	2685	1586
29	3	0.455	0.783	2723	1583
23	12	0.447	0.785	2771	1578
28	5	0.452	0.779	2746	1591
24	11	0.431	0.806	2880	1539
31	0	0.420	0.823	2953	1506
30	2	0.423	0.819	2934	1515
19	17	0.436	0.785	2843	1579
29	4	0.422	0.812	2936	1527
20	16	0.430	0.792	2882	1565
22	14	0.436	0.777	2842	1595
28	6	0.422	0.802	2936	1545
23	13	0.422	0.792	2935	1565
27	8	0.419	0.792	2959	1566
26	10	0.419	0.779	2960	1592
32	1	0.403	0.786	3080	1578

**4.2 Transparent Conductive Films Based on V$_2$O$_5$/SWCNTs**

The hydrolysis-polycondensation process of vanadyl triisopropoxide (VTIP) leading to the formation of vanadium oxide has a complex impact on SWCNT properties. As demonstrated by UV–vis-NIR spectroscopy studies (**Fig. 4.7a**), there are partial disappearances of transitions between Van Hove singularities (S$_{11}$, S$_{22}$, M$_{11}$), attributed to charge transfer effects induced by p-type doping with V$_2$O$_5$ [145,146]. Remarkably, the absorbance of the SWCNT film does not exhibit a significant increase upon the deposition of vanadium oxide. Additionally, doping results in a substantial reduction in the film sheet resistance [107], opening up opportunities for applications as an electrode in general and as a transparent electrode in particular.
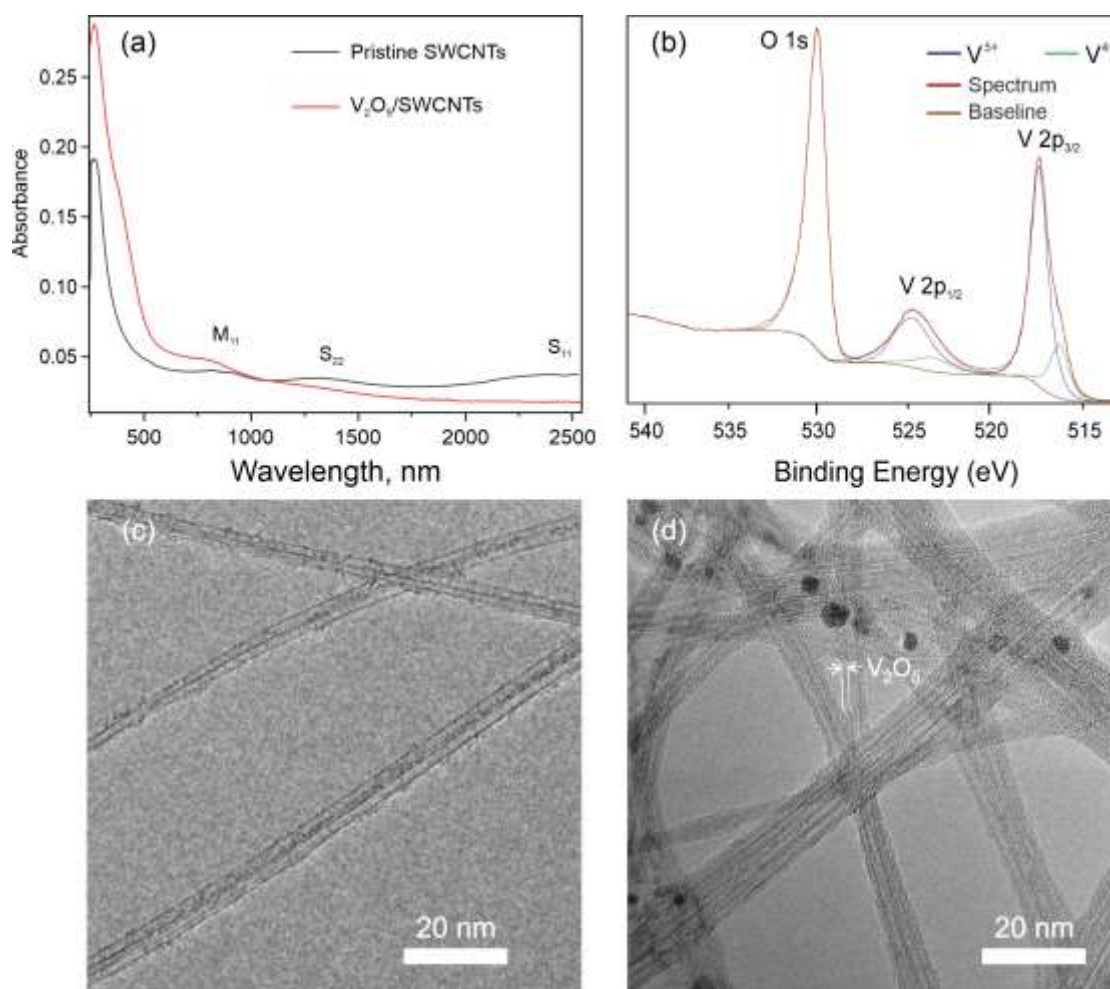
Figure 4.7. (a) UV-vis-NIR spectra of the pristine and V_2O_5-covered SWCNT films; (b) XPS spectrum (O 1s−V 2p region) of the V_2O_5/SWCNT composite material, (c) and (d) TEM images of pristine and V_2O_5-covered SWCNTs, respectively. Reproduced with permission[12]. Copyright 2023, The Royal Society of Chemistry.

XPS measurements confirm the exclusive presence of vanadium pentoxide on the surface of the SWCNTs (as depicted in **Fig. 4.7b**; the survey spectrum is presented in **Fig. 4.8a**). We observe characteristic peaks of V^{+5} at 517.2 eV (2p3/2) and 524.5 eV

(2p3/2). Furthermore, the peak corresponding to the trace amount of V^{+4} (2p3/2 at 516.0 eV) is observed to increase during exposure, likely attributed to the reduction of V^{+5} by X-ray irradiation [147].
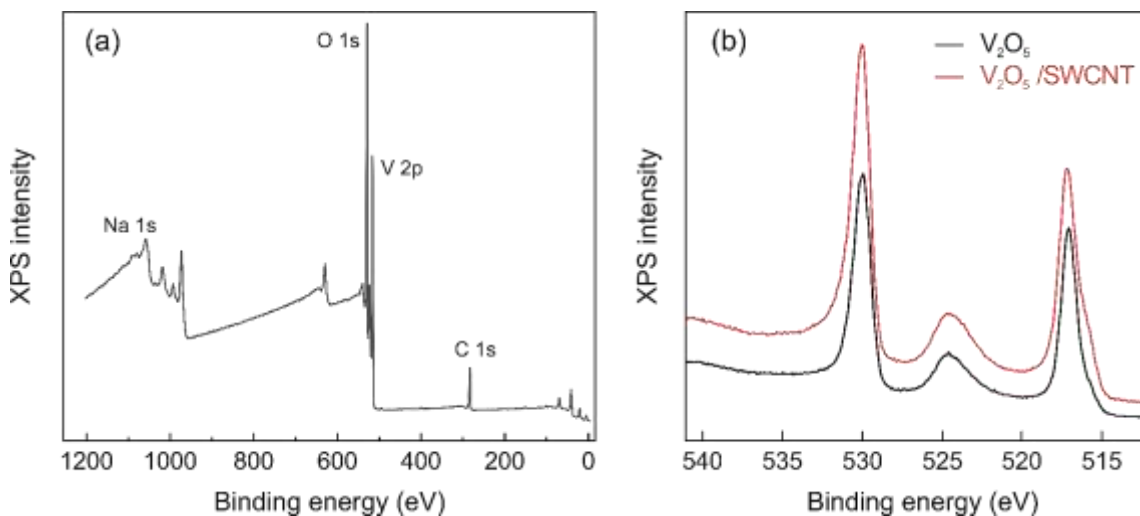

Figure 4.8a. XPS survey spectrum of the V_2O_5/SWCNT composite (a), a trace amount of Na (with an atomic concentration of about 1%) was found here as an impurity; O 1s−V 2p region of the bare V_2O_5 and V_2O_5/SWCNT composite material (b). Reproduced with permission [12]. Copyright 2023, The Royal Society of Chemistry.

The O 1s−V 2p region of bare V_2O_5 closely matches the same region for the V_2O_5/SWCNT composite, providing evidence that the interaction between carbon nanotubes and vanadium oxide is primarily physical (**Fig. 4.8b**). We conducted TEM observations to investigate the morphology of the V_2O_5/SWCNT composite, with pristine SWCNTs serving as the reference (**Fig. 4.7c**). Our findings revealed a homogeneous deposition of a thin vanadium oxide film on the surface of SWCNTs (**Fig. 4.7d**). This deposition can be attributed to the efficient wetting of the SWCNT surface by

55

isopropanol, which serves as the solvent for VTIP. The thickness of the layer around the SWCNTs is estimated to be approximately 1 nm and appears amorphous, consistent with XRD measurements (**Fig. 4.9a, b**) and selected area electron diffraction of the V_2O_5/SWCNT composites. In the diffraction pattern, there are no rings corresponding to crystalline phases, suggesting an amorphous structure [148]. It's worth noting that the thickness of the V_2O_5 layer can be adjusted by varying the concentration of the VTIP solution. TEM morphology of materials doped with 0, 9, and 42 µM solutions is presented in **Fig. 4.9c-e**.

To elucidate the peculiarities of the hydrolysis-polycondensation mechanism, we examined the influence of process conditions such as temperature and humidity. We utilized R_s of the composites as a non-invasive parameter to monitor the evolution of materials and the interaction between SWCNTs and V_2O_5. Following the spin coating of VTIP/isopropanol onto the SWCNT films, we observed an immediate drop in sheet resistance to a value denoted as R_0. We observed a consistent and approximately 30% increase in sheet resistance over the first month (red curve in **Fig. 4.10a**). Subsequent observations over the next two months revealed no further changes, demonstrating the stability of doping over time. Interestingly, the evolution pattern exhibited no correlation with the amount of vanadium oxide (blue curve in **Fig. 4.10a**) or the presence of water or oxygen during storage (violet curve in **Fig. 4.10a**).
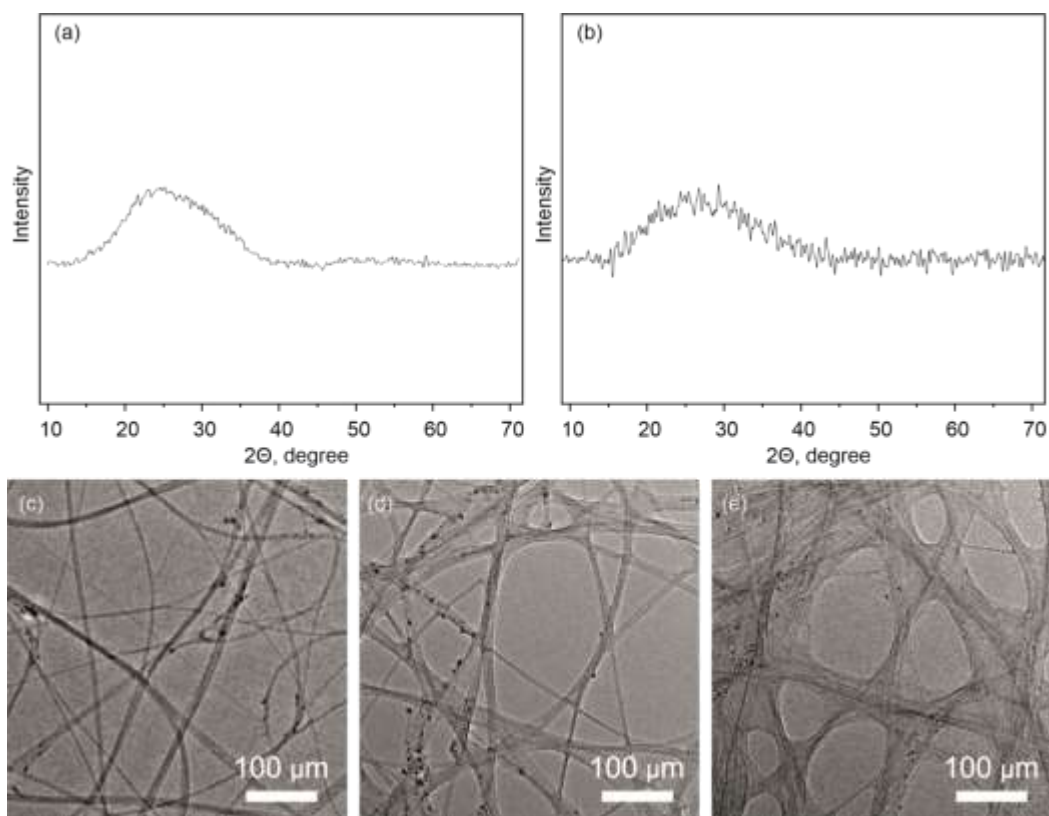
Figure 4.9. XRD patterns of the pristine SWCNT film (a) and V_2O_5/SWCNT composite (b), TEM images of SWCNTs doped by 0 (c), 9 (,d) and 42 (e) μM solution of VTIP. TEM images reveal iron nanoparticles – active and inactive catalyst formed due to the decomposition of ferrocene. Reproduced with permission[12]. Copyright 2023, The Royal Society of Chemistry.

When we elevated the temperature to 35°C (green curve in **Fig. 4.10b**) or 60°C (navy curve in **Fig. 4.10b**), we observed a similar 30% increase in resistance values but within significantly shorter durations, specifically 60 and 5 minutes, respectively. This rapid change in the reaction rate for the chemical process corresponds to an apparent activation energy of approximately 190 kJ/mol.
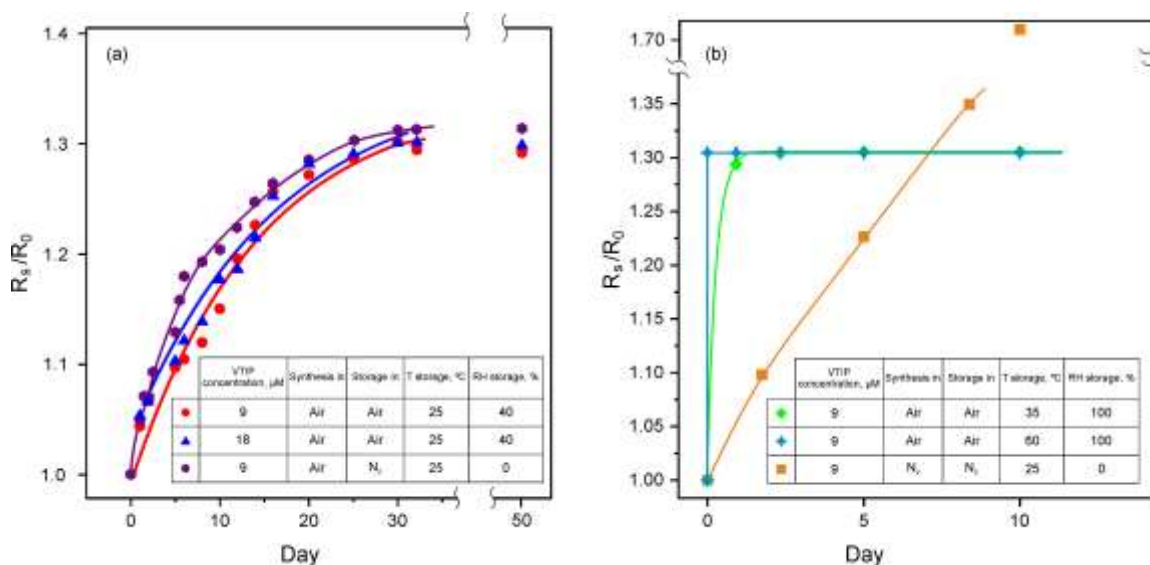
Figure 4.10. Time evolution of normalized sheet resistance (R_0 is the initial sheet resistance) of the V_2O_5/SWCNT composite under different conditions: (a) at 25°C and 40% RH, (b) increased temperature and RH, and the test of VTIP/V_2O_5 material. Reproduced with permission [12]. Copyright 2023, The Royal Society of Chemistry.

When an SWCNT film was spin-coated with a VTIP solution (9 µM) inside a nitrogen glovebox with extremely low levels of water and oxygen (< 0.1 ppm), we observed a substantial doping effect on the SWCNTs, resulting in a sheet resistance of $R_{90} = 130\ \Omega$ sq^{-1}. This is notably lower than the equivalent sheet resistance of 330 Ω sq^{-1} observed in the undoped film. However, the evolution pattern of sheet resistance under a nitrogen environment differs (as indicated by the orange curve in **Fig. 4.10b**); in this case, the R_s value steadily increases. This phenomenon can be attributed to the evaporation of liquid VTIP without the formation of V_2O_5, as there is an absence of water-induced hydrolysis in the system.

This observation allows us to elucidate the mechanism of V_2O_5 formation from the VTIP solution. During the spin-coating process (as depicted in **Fig. 3.3**), isopropanol covers the nanotubes and subsequently evaporates from the SWCNT surface. Simultaneously, VTIP reacts with water vapor present in the air, leading to the formation of the vanadium oxide coating. The simplified general reaction of complete hydrolysis of VTIP is [149]:

$$2VO(O - iPr)_3 + 3H_2O \rightarrow V_2O_5 + 6iPrOH. \tag{4.20}$$
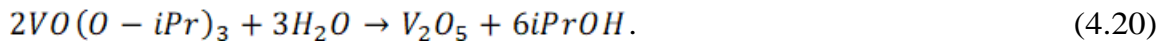
The VTIP/isopropanol solution has been observed to enhance the conductivity of SWCNT films, as evident from the orange curve in **Fig. 4.10b**, where V_2O_5 formation did not occur. The rate of the hydrolysis-polycondensation reaction is notably temperature-dependent, with an estimated activation energy of approximately 190 kJ/mol, as indicated by the temperature-dependent sheet resistance in **Fig. 4.10** at 25, 35, and 60°C. This value is likely associated with the hydrolysis reaction, which is likely the slowest step of the process [150]. In a prior study [151], the synthesis of V_2O_5 exhibited an activation energy that was approximately half of this value, possibly attributed to different precursors and the presence of a catalyst.
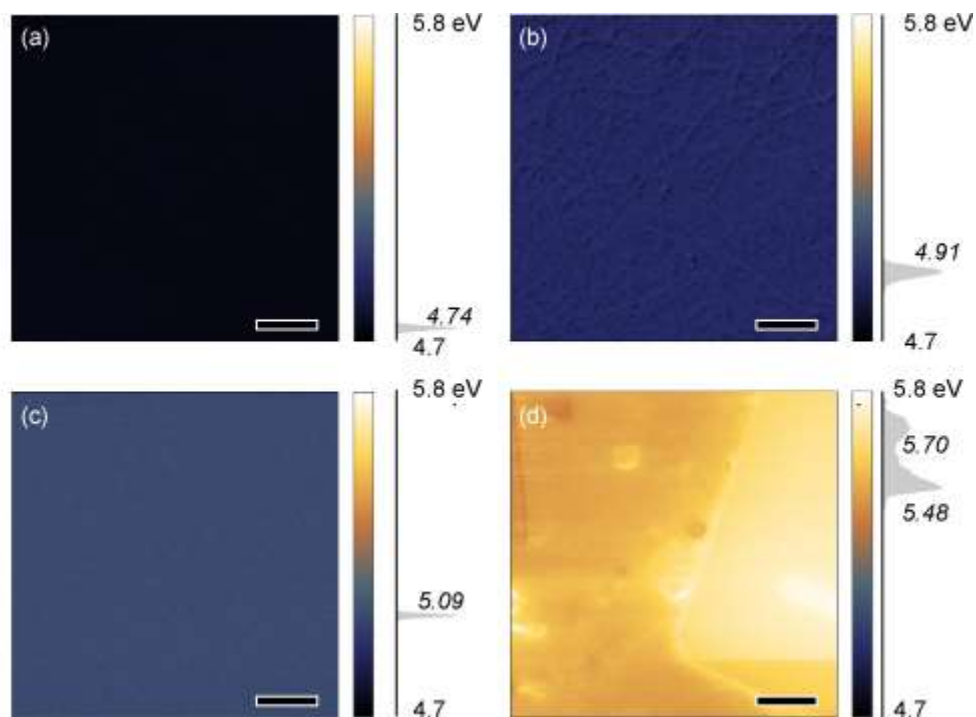
Figure 4.11. Results of Kelvin Probe Force Microscopy showing the work function map for (a) V_2O_5 deposited from VTIP solution, (b) the V_2O_5/SWCNT composite, (c) V_2O_5 deposited by thermal sputtering, (d) V_2O_5 deposited from VTIP solution and annealed at 600ºC in the air (scale bar is 1 µm). Reproduced with permission [12]. Copyright 2023, The Royal Society of Chemistry.

V_2O_5 is known for its notably high work function, reaching up to 7.0 eV [152], making it suitable for a wide range of applications, including gas sensors, heterogeneous catalysts, organic photovoltaic devices, and organic light-emitting diodes, among others [145,146,152]. When applied to a SWCNT film, a material with a high work function can effectively enhance conductivity through the doping process [153]. To assess the work function of the obtained materials, we conducted Kelvin Probe Force Microscopy

60

measurements (**Fig. 4.11**). Pristine V_2O_5 deposited from a 9-µM VTIP solution exhibited a relatively low work function, approximately 4.8 eV (**Fig. 4.11a**). Consequently, the thin layer of V_2O_5 on the surface of SWCNTs did not significantly alter the overall work function of the composite (**Fig. 4.11b**) in comparison to pristine SWCNTs (approximately 4.8 eV). As a reference, we measured the work function for a thermally-sputtered 30-nm V_2O_5 layer, which also hovered around 5 eV (**Fig. 4.11c**). Thus, thin amorphous layers of V_2O_5 obtained through hydrolysis-polycondensation and thermal evaporation methods exhibit relatively low work functions, which can be increased to 5.8 eV through sample annealing at 600°C (**Fig. 4.11d**), resulting in the emergence of a crystalline phase. However, this process led to non-uniform films, potentially introducing defects into the SWCNT structure. These findings align with in situ XRD studies, where no additional reflections were observed after V_2O_5 deposition (**Fig. 4.12**), while subsequent heating in an "air" environment revealed recrystallization into a mixture of phases, most likely orthorhombic and monoclinic, following nanotube burning (**Fig. 4.13**). The presence of a thin amorphous layer of V_2O_5 effectively enhances the conductivity of the SWCNT film. This enhancement may result from charge exchange between SWCNTs and absorbed oxide molecules, leading to p-type doping [145,146]. Additionally, the V_2O_5 layer can serve as a protective barrier for SWCNTs, mitigating the environmental impact on their characteristics.
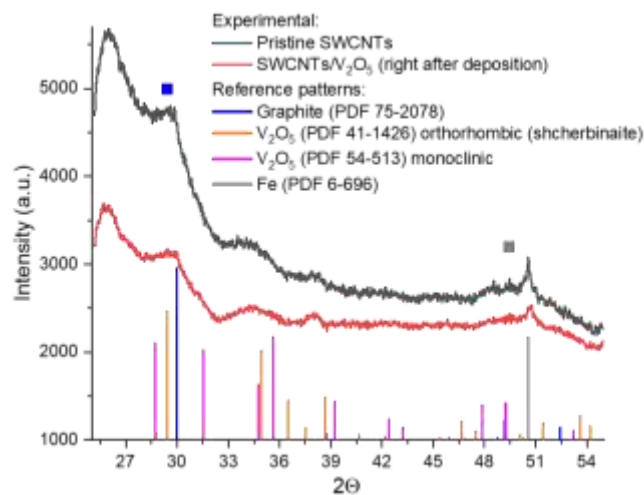
Figure 4.12. Typical in situ XRD patterns of pristine SWCNTs (black) and the same SWCNTs covered with V_2O_5 (red); database PDF patterns of graphite (blue), V_2O_5 (orthorhombic (orange), and monoclinic (magenta)), and iron (grey). Reproduced with permission [12]. Copyright 2023, The Royal Society of Chemistry.

V_2O_5 is regarded as a promising dopant for SWCNTs due to its ability to form thin layers with high transmittance and induce p-type doping effects [145,146]. When the VTIP concentration is varied from 1 to 60 µM, it results in changes in the equivalent sheet resistance of transparent conductive films, showing an extremum point (**Fig. 4.15a**). Notably, at a concentration of 9 µM, the lowest R_{90} value of 130 Ω/sq is achieved. The equivalent sheet resistance reflects a trade-off balance between the sample's conductivity. Up to the 9 µM concentration, there is no significant alteration in the transmittance of the samples, while the resistance gradually decreases.
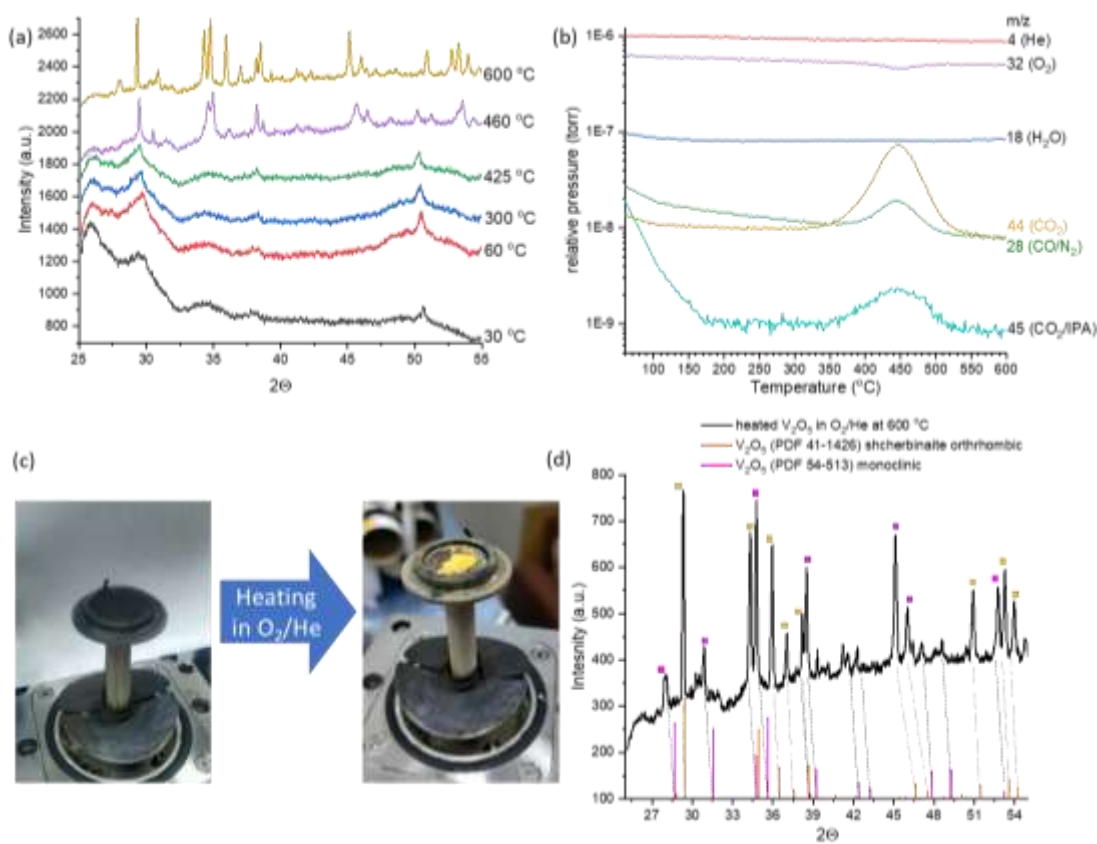
Figure 4.13. *In situ* XRD patterns of V_2O_5/SWCNT during heating in "air" (a); temperature dependence of designated m/z signals of the mass spectrometer with the proposed gas species; photos of the XRD holder before and after heating in the air; in situ XRD pattern of the sample heated at 600 °C in "air"(d). Reproduced with permission [12]. Copyright 2023, The Royal Society of Chemistry.

We propose that at lower concentrations, specifically up to 9 µM, the equivalent sheet resistance experiences a noticeable decrease due to the coverage of SWCNTs by the precursor. However, increasing the VTIP concentration beyond this point does not significantly contribute to the composite's conductivity. Instead, it results in a further

reduction in transmittance due to the additional V_2O_5 layer formation. We achieved an impressive equivalent sheet resistance of R_{90} = 130 Ω sq^{-1} (**Fig. 4.15a**), which ranks among the lowest values for metal oxide doping.

To assess doping stability, we conducted a comparative test between SWCNTs doped with the highly effective dopant $HAuCl_4$ and those with the V_2O_5 layer prepared using our method [113]. For the $HAuCl_4$-doped samples (using a 30 µM solution in isopropanol), the resistance increased by 90% at 25°C and 40% RH (**Fig. 4.15b**). In contrast, for the V_2O_5-doped samples pre-heated to 60ºC for 5 minutes (using a 9 µM solution in isopropanol), the resistance increased by only 30% (by the complete transformation discussed earlier) under the same conditions. This observation demonstrates that the composite exhibits remarkable stability in its optoelectronic properties.

In summary, the coating of SWCNT films with a VTIP solution at ambient conditions offers a highly stable doping method for SWCNTs. The observed 30% drop in conductivity can be attributed to the completion of the hydrolysis-polycondensation reaction. As a result, the V_2O_5/SWCNT composite consistently maintains an equivalent sheet resistance of R_{90} = 160 Ω sq^{-1}, showcasing its stability in optoelectronic properties.
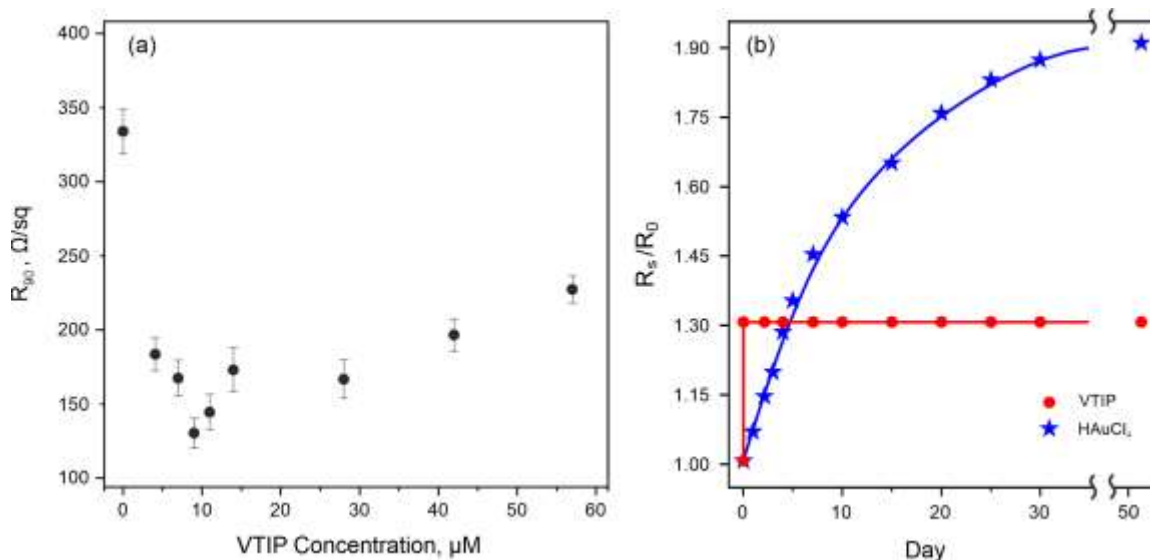
Figure 4.15. V_2O_5/SWCNT composite as transparent conductive films: (a) concentration of dopant precursor *vs* equivalent sheet resistance for an SWCNT/V_2O_5 transparent conductive film with the size of 1 cm^2; (b) stability of the conductivity for SWCNT-based for transparent conductive films covered by V_2O_5 and HAuCl$_4$. Reproduced with permission [12]. Copyright 2023, The Royal Society of Chemistry.

4.3 Fundamental Limit for SWCNT-Based TCF

This chapter is dedicated to the concept of an ideal SWCNT network designed to achieve the highest optoelectronic performance, establishing the fundamental threshold for TCFs based on SWCNTs. To formulate this concept, we need to create a conductive network devoid of charge carrier hopping and scattering. For this purpose, consider a film comprised of parallel, defect-free SWCNTs (**Figure 4.16a**). This type of network inherently provides conductivity in only one direction. We determined the electrical conductivity of individual SWCNTs by evaluating the transmission coefficient using the

Landauer–Buttiker formalism, employing the Keldysh nonequilibrium Green function technique, along with a novel approach for expediting transmission coefficient calculations [154].

To create a non-unidirectional conducting surface, the film should consist of at least two layers, positioned at a 90º angle to each other, as shown in **Figure 4.16b**. These two configurations are expected to yield the best TCF performance for unidirectional and bi-directional networks, provided that suitable components are chosen. Notably, SWCNTs outperform double-walled and multi-walled CNTs in terms of optical transmittance at the same current density [155]. Armchair SWCNTs exhibit ballistic conductance and possess minimal resistance, with a quantum resistance of 6.46 kΩ among other configurations [156].

To calculate the electrical conductivity of individual SWCNTs, we employed the transmission coefficient according to the Landauer–Buttiker formalism, utilizing the Keldysh nonequilibrium Green function technique and an original method for accelerating transmission coefficient calculations [154]. We constructed a film of aligned armchair SWCNTs as parallel-connected resistors (**Figure 4.16c**). In this case, the resistance of the film can be estimated as:

$$\frac{1}{R} = \Sigma \frac{1}{R_i},$$
(4.21)

$$R = R_{SWCNT}/n.$$
(4.22)

Here, n represents the number of SWCNTs in a film, and R_{SWCNT} is the resistance of a single SWCNT.
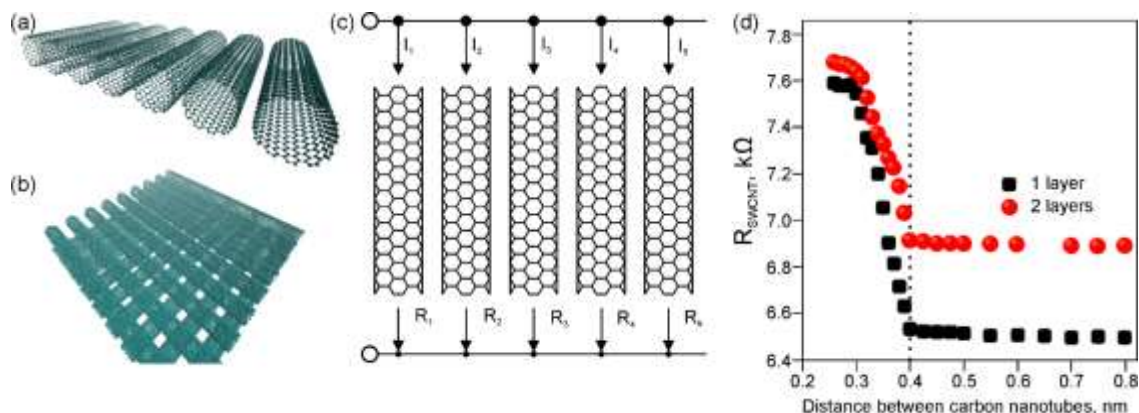
Figure 4.16. Ideal SWCNT-based TCFs: (a) 1-layer and (b) 2-layer films based on armchair SWCNTs; (c) equivalent circuit of the film of aligned SWCNTs; (d) resistance of one SWCNT in equivalent circuit in the dependence on the distance between SWCNTs. Reproduced with permission [1]. Copyright 2022, Wiley.

Figure 4.16d illustrates the dependence of SWCNT resistance on the gap between tubes. When the distance is too small, the overlap of π electronic clouds leads to an increase in resistance. However, as the distance between nanotubes exceeds 4 Å, the interaction of electronic clouds disappears, and the resistance decreases to the quantum resistance value for a SWCNT in a monolayer film. Importantly, this resistance remains independent of the diameter of SWCNTs. For a double-layered TCF, the minimal resistance is slightly higher (6.84 kΩ) due to the contact between layers and the scattering of charge carriers. In this ideal defect-free model, these resistance values remain constant within the realm of ballistic transport, regardless of the length of nanotubes.
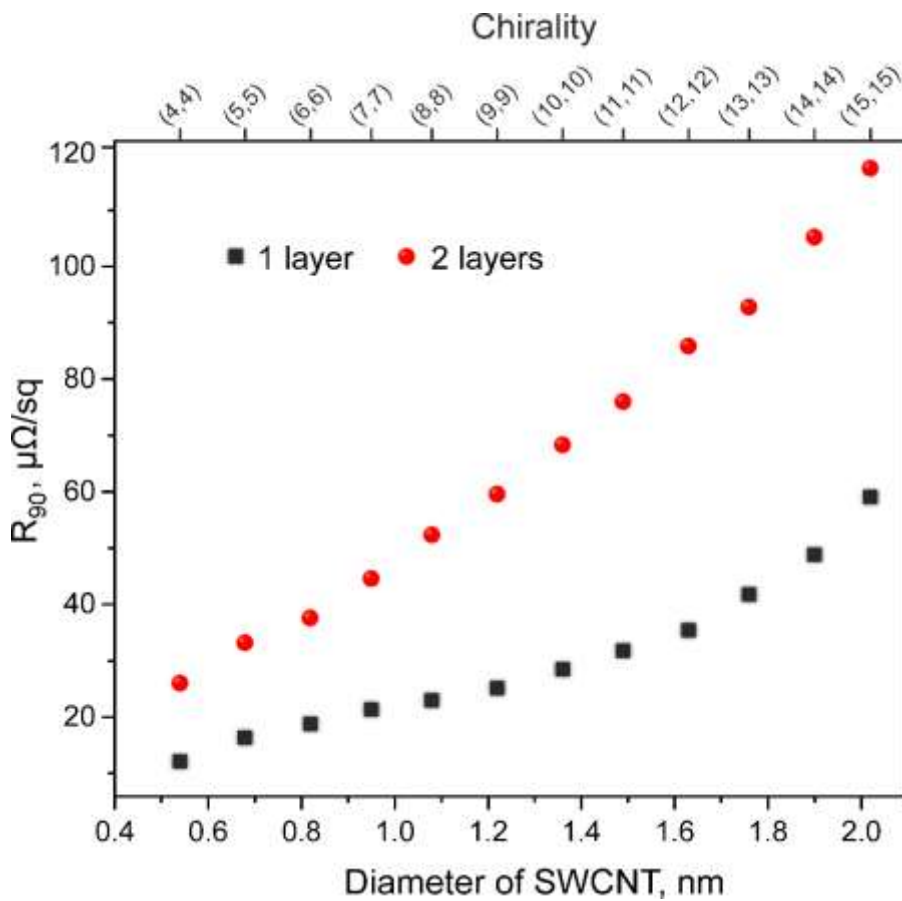
Figure 4.17. Dependence of R$_{90}$ on chirality/diameter of SWCNTs in case of ideal films of ordered "armchair" SWCNTs. Reproduced with permission [1]. Copyright 2022, Wiley.

In our emulation of real-size devices employing TCFs, we conducted R_{90} calculations for films with dimensions of 10×10 cm^2. We estimated the number of nanotubes that can be placed along a 10 cm length at a distance of 4 Å between each other. The results of the calculations, considering Eq. (4.21) and accounting for the absorbance at a 550 nm wavelength for 1- and 2-layer films, are presented in **Figure 4.17**. Such films possess R_{90} of $\mu\Omega$ sq^{-1} order of magnitude, while the smaller the

diameter of the SWCNTs, the more nanotubes can be accommodated to create a TCF. Films consisting of (4,4) SWCNTs exhibit the best possible characteristics for TCFs, with R_{90} values of 14 and 22 $\mu\Omega$ sq^{-1} for 1D- and 2D-conducting films, respectively. These values can be regarded as the fundamental limits for the optoelectronic performance of SWCNT-based films.

In conclusion, transparent electrodes based on carbon nanotubes have enormous potential for enhancement, potentially surpassing all known materials, including ITO and metal films. This work unveils the fundamental threshold for TCFs based on SWCNTs, opening up new and promising horizons for the advancement of this field.

Conclusions

In the frames of this work, we improved the optoelectronic performance of SWCNT films during the material fabrication by implementing a rational design approach at both deposition and post-deposition stages.

In the framework of the deposition approach, we have introduced a novel method for the direct precipitation of SWCNTs from an aerosol flow, leveraging the principle of photophoretic motion induced by irradiation from various light sources. Our proposed method enables the efficient deposition of carbon nanotubes on a quartz substrate using a 6.0 W LED lamp, achieving an impressive deposition efficiency of 10%. This result aligns well with our developed theoretical model, which is grounded in the photophoretic velocity of both spherical and cylindrical particles. By adjusting the deposition time, we can conveniently produce various SWCNT configurations, ranging from individual species to small bundles and even continuous networks. Raman spectra in the RBM region reveal intensity redistributions among different chiralities when irradiation is present, likely due to variations in the photophoretic asymmetry factors of SWCNTs, indicating partial selectivity. Furthermore, deposition under 1550 nm laser irradiation demonstrates the saturation of photoluminescence in the 1500-1600 nm range, providing qualitative evidence of chiral selectivity. Our photophoretic deposition method opens up new avenues for directly separating carbon nanotubes and holds potential applications, including the production of single-photon sources using individual nanotubes or patterned films for semiconducting SWCNT networks. This innovation marks a significant advancement in the field of SWCNT manipulation and utilization.

In the frames of the doping approach, we have introduced an innovative, straightforward, and rapid technique for applying a uniform and continuous layer of V_2O_5 with adjustable thickness onto SWCNTs. This method leverages the synthesis process based on the hydrolysis-polycondensation mechanism, which occurs on the surface of SWCNTs, utilizing vanadyl triisopropoxide as the precursor. Our analyses confirm that the resulting coating is composed of amorphous vanadium pentoxide with a work function of 4.8 eV. This work function can be enhanced to 5.8 eV through high-temperature recrystallization at 600ºC. Consequently, we have successfully produced films with an equivalent sheet resistance of 160 Ω sq^{-1} (at T = 90%), ranking among the top performers for metal-oxide doping of carbon nanotubes. The stability of the optoelectronic properties of the films was approved by climatic tests. We anticipate that our method, which enables the creation of a thin V_2O_5 layer around SWCNTs and other substrates, will find valuable applications across various fields, including electrochemistry, optoelectronics, and photovoltaics.

Drawing upon rational design principles, we have examined the pathway for the future advancement of TCF materials. As part of this exploration, we engineered an ideal SWCNT network and conducted calculations to determine the optimal performance. Specifically, we have identified the theoretical limits for TCFs based on unidirectional and two-layered SWCNT conducting films, yielding sheet resistances of R_{90} = 14 and 22 $\mu\Omega$ sq^{-1}, respectively. These remarkably low sheet resistance values underscore the vast potential for further advancement in the realm of transparent conductors based on SWCNTs.

71

Bibliography

1. Ilatovskii D.A. et al. Transparent Conducting Films Based on Carbon Nanotubes : Rational Design toward the Theoretical Limit // Adv. Sci. 2022. Vol. 2201673. P. 1–16.

2. Chae S.H., Lee Y.H. Carbon nanotubes and graphene towards soft electronics // Nano Converg. 2014. Vol. 1, № 1. P. 1–26.

3. Zhang Q. et al. Recent Developments in Single-Walled Carbon Nanotube Thin Films Fabricated by Dry Floating Catalyst Chemical Vapor Deposition // Top. Curr. Chem. Springer International Publishing, 2017. Vol. 375, № 6. P. 1–30.

4. Zhou Y., Azumi R. Carbon nanotube based transparent conductive films: progress, challenges, and perspectives // Sci. Technol. Adv. Mater. Taylor & Francis, 2016. Vol. 17, № 1. P. 493–516.

5. Ivanov, I.N., Garrett, M.P., Gerhardt R.A. Carbon Nanotube Assemblies for Transparent Conducting Electrodes // Nanoscale Applications for Information and Energy Systems. 2013. № Mi. 117–147 p.

6. López-Naranjo E.J. et al. Transparent Electrodes: A Review of the Use of Carbon-Based Nanomaterials // J. Nanomater. 2016. Vol. 2016. P. 1–12.

7. Jiang S. et al. High-performance single-wall carbon nanotube transparent conductive films // J. Mater. Sci. Technol. The editorial office of Journal of Materials Science & Technology, 2019. Vol. 35, № 11. P. 2447–2462.

8. Khabushev E.M. et al. Machine Learning for Tailoring Optoelectronic Properties of Single-Walled Carbon Nanotube Films // J. Phys. Chem. Lett. 2019. Vol. 10, №

21. P. 6962–6966.

9. Iakovlev V.Y. et al. Artificial neural network for predictive synthesis of single-walled carbon nanotubes by aerosol CVD method // Carbon N. Y. 2019. Vol. 153. P. 100–103.

10. Kaskela A. et al. Aerosol-synthesized SWCNT networks with tunable conductivity and transparency by a dry transfer technique // Nano Lett. 2010. Vol. 10, № 11. P. 4349–4355.

11. Rubinowicz A. Radiometerkräfte und Ehrenhaftsche Photophorese // Ann. Phys. 1920. Vol. 367, № 16. P. 716–737.

12. Ilatovskii D.A. et al. Robust method for uniform coating of carbon transparent electrodes and Li-ion batteries †. Royal Society of Chemistry, 2023. P. 25817–25827.

13. Yu L. et al. Insights into chemical doping to engineer the carbon nanotube/silicon photovoltaic heterojunction interface // J. Mater. Chem. A. 2017. Vol. 5, № 46. P. 24247–24256.

14. Kopylova D.S. et al. Electrochemical enhancement of optoelectronic performance of transparent and conducting single-walled carbon nanotube films // Carbon N. Y. Elsevier Ltd, 2020. Vol. 167. P. 244–248.

15. Chouhan A.S., Jasti N.P., Avasthi S. The dual role of ozone-treated aluminum doped zinc oxide for CH3NH3PbI3 solar cells // Org. Electron. physics, Mater. Appl. Elsevier, 2019. Vol. 66, № August 2018. P. 249–257.

16. Funde A.M., Nasibulin A.G., Syed H.G. Carbon nanotube – amorphous silicon

hybrid solar cell with improved conversion ef fi ciency // Nanotechnology. IOP Publishing, 2016. Vol. 27. P. 185401.

17. Kim S., Shin S.H., Choi S.H. N-i-p-type perovskite solar cells employing n-type graphene transparent conductive electrodes // J. Alloys Compd. Elsevier B.V, 2019. Vol. 786. P. 614–620.

18. Kwak S.W. et al. Solution-shearing-processed flexible polymer solar mini sub-modules fabricated on an embedded silver-grid substrate // Sol. Energy Mater. Sol. Cells. Elsevier B.V., 2019. Vol. 193, № November 2018. P. 169–177.

19. Pang S. et al. Graphene as transparent electrode material for organic electronics // Adv. Mater. 2011. Vol. 23, № 25. P. 2779–2795.

20. Rajanna P.M. et al. Enhanced efficiency of hybrid amorphous silicon solar cells based on single-walled carbon nanotubes and polymer composite thin film // Nanotechnology. IOP Publishing, 2018. Vol. 29, № 10. P. 105404.

21. Will P.-A., Reineke S. Organic light-emitting diodes // Handb. Org. Mater. Electron. Photonic Devices. 2019. Vol. 4, № 1. P. 695–726.

22. Dong H. et al. A Flexible and Thin Graphene/Silver Nanowires/Polymer Hybrid Transparent Electrode for Optoelectronic Devices // ACS Appl. Mater. Interfaces. 2016. Vol. 8, № 45. P. 31212–31221.

23. Kim E. et al. Ag fiber/IZO Composite Electrodes: Improved Chemical and Thermal Stability and Uniform Light Emission in Flexible Organic Light-Emitting Diodes // Sci. Rep. Springer US, 2019. Vol. 9, № 1. P. 3–9.

24. Kumar N. et al. Flexible transparent conducting electrodes based on metal meshes

for organic optoelectronic device applications: a review // J. Mater. Chem. C. Royal Society of Chemistry, 2018. Vol. 7, № 5. P. 1087–1110.

25. Vinogradov A. V. et al. The first depleted heterojunction TiO2-MOF-based solar cell // Chem. Commun. Royal Society of Chemistry, 2014. Vol. 50, № 71. P. 10210–10213.

26. Yamamoto N. et al. Development of Ga-doped ZnO transparent electrodes for liquid crystal display panels // Thin Solid Films. Elsevier B.V., 2012. Vol. 520, № 12. P. 4131–4138.

27. Park Y. et al. Fabrication of New Liquid Crystal Device Using Layer-by-Layer Thin Film Process // Processes. 2018. Vol. 6, № 8. P. 108.

28. Hong S. et al. Nonvacuum, Maskless Fabrication of a Flexible Metal Grid Transparent Conductor by Low-Temperature Selective Laser Sintering of Nanoparticle Ink // ACS Nano. 2013. Vol. 7, № 6. P. 5024–5031.

29. He L., Tjong S.C. Nanostructured transparent conductive films: Fabrication, characterization and applications // Mater. Sci. Eng. R Reports. Elsevier B.V., 2016. Vol. 109. P. 1–101.

30. Cho S. et al. Large-Area Cross-Aligned Silver Nanowire Electrodes for Flexible, Transparent, and Force-Sensitive Mechanochromic Touch Screens // ACS Nano. 2017. Vol. 11, № 4. P. 4346–4357.

31. Chu H.C. et al. Spray-Deposited Large-Area Copper Nanowire Transparent Conductive Electrodes and Their Uses for Touch Screen Applications // ACS Appl. Mater. Interfaces. 2016. Vol. 8, № 20. P. 13009–13017.

32. Gilshteyn E.P. et al. A One-Step Method of Hydrogel Modification by Single-Walled Carbon Nanotubes for Highly Stretchable and Transparent Electronics // ACS Appl. Mater. Interfaces. 2018. Vol. 10, № 33. P. 28069–28075.

33. Cai L. et al. Super-stretchable, transparent carbon nanotube-based capacitive strain sensors for human motion detection // Sci. Rep. 2013. Vol. 3. P. 1–9.

34. Shinya Aikawa et al. Deformable transparent all-carbon-nanotube transistors // Appl. Phys. Lett. 2012. Vol. 100. P. 063502.

35. Luo M. et al. Towards flexible transparent electrodes based on carbon and metallic materials // Micromachines. 2017. Vol. 8, № 1. P. 1–16.

36. Bhosle V., Tiwari A., Narayan J. Electrical properties of transparent and conducting Ga doped ZnO // J. Appl. Phys. 2006. Vol. 100, № 3.

37. Hitosugi T. et al. Properties of TiO2-based transparent conducting oxides // Phys. Status Solidi Appl. Mater. Sci. 2010. Vol. 207, № 7. P. 1529–1537.

38. Turgut G. et al. Effect of Nb doping on structural, electrical and optical properties of spray deposited SnO2 thin films // Superlattices Microstruct. 2013. Vol. 56. P. 107–116.

39. Cairns D.R. et al. Strain-dependent electrical resistance of tin-doped indium oxide on polymer substrates // Appl. Phys. Lett. 2000. Vol. 76, № 11. P. 1425–1427.

40. Brewer S.H., Franzen S. Indium tin oxide plasma frequency dependence on sheet resistance and surface adlayers determined by reflectance FTIR spectroscopy // J. Phys. Chem. B. 2002. Vol. 106, № 50. P. 12986–12992.

41. Gao M.Z. et al. Thickness dependence of resistivity and optical reflectance of ITO

films // Chinese Phys. Lett. 2008. Vol. 25, № 4. P. 1380–1383.

42. Greenbank W. et al. Interfacial thermal degradation in inverted organic solar cells // Appl. Phys. Lett. 2015. Vol. 107, № 26.

43. Ghosh D.S. et al. Widely transparent electrodes based on ultrathin metals // Opt. Lett. 2009. Vol. 34, № 3. P. 325.

44. Schneider J. et al. Electrohydrodynamic NanoDrip Printing of High Aspect Ratio Metal Grid Transparent Electrodes // Adv. Funct. Mater. 2016. Vol. 26, № 6. P. 833–840.

45. He W., Ye C. Flexible Transparent Conductive Films on the Basis of Ag Nanowires: Design and Applications: A Review // J. Mater. Sci. Technol. Elsevier Ltd, 2015. Vol. 31, № 6. P. 581–588.

46. Hatton R.A. et al. A robust ultrathin, transparent gold electrode tailored for hole injection into organic light-emitting diodes // J. Mater. Chem. 2003. Vol. 13, № 4. P. 722–726.

47. Im H. et al. Template-stripped smooth Ag nanohole arrays with silica shells for surface plasmon resonance biosensing // ACS Nano. 2011. Vol. 5, № 8. P. 6244–6253.

48. Anoshkin I. V. et al. Resistivity and optical transmittance dependence on length and diameter of nanowires in silver nanowire layers in application to transparent conductive coatings // Micro Nano Lett. 2016. Vol. 11, № 7. P. 343–347.

49. Daneshvar F. et al. Ultralong Electrospun Copper-Carbon Nanotube Composite Fibers for Transparent Conductive Electrodes with High Operational Stability //

ACS Appl. Electron. Mater. 2020. Vol. 2, № 9. P. 2692–2698.

50. Hofmann A.I., Cloutet E., Hadziioannou G. Materials for Transparent Electrodes: From Metal Oxides to Organic Alternatives // Adv. Electron. Mater. 2018. Vol. 4, № 10. P. 1700412.

51. Eckhardt S., Siebold M., Lasagni A.F. Laser microstructured metal thin films as promising alternative for indium based transparent electrodes // Opt. Express. 2016. Vol. 24, № 6. P. A553.

52. Chen Z. et al. One-Step Growth of Graphene/Carbon Nanotube Hybrid Films on Soda-Lime Glass for Transparent Conducting Applications // Adv. Electron. Mater. 2017. Vol. 3, № 11. P. 1–8.

53. Chen Y., Gong X.L., Gai J.G. Progress and Challenges in Transfer of Large-Area Graphene Films // Adv. Sci. 2016. Vol. 3, № 8. P. 1–15.

54. Gordon R.G. Criteria for Choosing Transparent Conductors Materials Properties Relevant to Transparent Conductors Optical and Electrical Performance of Transparent Conductors // MRS Bull. 2011. Vol. 25, № 8. P. 52–57.

55. Anoshkin I. V. et al. Hybrid carbon source for single-walled carbon nanotube synthesis by aerosol CVD method // Carbon N. Y. Elsevier Ltd, 2014. Vol. 78. P. 130–136.

56. Wu Z. et al. Transparent, conductive carbon nanotube films // Science (80-.). 2004. Vol. 305, № 5688. P. 1273–1276.

57. Moisala A. et al. Single-walled carbon nanotube synthesis using ferrocene and iron pentacarbonyl in a laminar flow reactor // Chem. Eng. Sci. 2006. Vol. 61, № 13. P.

4393–4402.

58. Nasibulin A.G. et al. Integration of single-walled carbon nanotubes into polymer films by thermo-compression // Chem. Eng. J. 2008. Vol. 136, № 2–3. P. 409–413.

59. Mikheev G.M. et al. Improvement of optoelectronic properties of single-walled carbon nanotube films by laser treatment // Diam. Relat. Mater. Elsevier, 2018. Vol. 88, № July. P. 144–150.

60. Romanov S.A. et al. Rapid, efficient, and non-destructive purification of single-walled carbon nanotube films from metallic impurities by Joule heating // Carbon N. Y. 2020. Vol. 168. P. 193–200.

61. Liao Y. et al. Direct Synthesis of Colorful Single-Walled Carbon Nanotube Thin Films: rapid-communication // J. Am. Chem. Soc. American Chemical Society, 2018. Vol. 140, № 31. P. 9797–9800.

62. Tian Y. et al. Growth of single-walled carbon nanotubes with controlled diameters and lengths by an aerosol method // Carbon N. Y. Elsevier Ltd, 2011. Vol. 49, № 14. P. 4636–4643.

63. Tsapenko A.P. et al. Highly conductive and transparent films of HAuCl4-doped single-walled carbon nanotubes for flexible applications // Carbon N. Y. 2018. Vol. 130. P. 448–457.

64. Hussain A. et al. Floating catalyst CVD synthesis of single walled carbon nanotubes from ethylene for high performance transparent electrodes // Nanoscale. Royal Society of Chemistry, 2018. Vol. 10, № 20. P. 9752–9759.

65. Jiang S. et al. Ultrahigh-performance transparent conductive films of carbon-

welded isolated single-wall carbon nanotubes // Sci. Adv. 2018. Vol. 4, № 5. P. eaap9264.

66. Nasibulin A.G. et al. Multifunctional Free-Standing Single-Walled Carbon Nanotube Films // ACS Nano. 2011. Vol. 5, № 4. P. 3214–3221.

67. Fedorov F.S. et al. High Performance Hydrogen Evolution Reaction Catalyst Based on Single-Walled Carbon Nanotubes Decorated by RuOx Nanoparticles // ChemElectroChem. 2020. Vol. 7, № 12. P. 2651–2659.

68. Sun D.M. et al. All-Carbon Thin-Film Transistors as a Step Towards Flexible and Transparent Electronics // Adv. Electron. Mater. 2016. Vol. 2, № 11. P. 1–22.

69. Yamada T. et al. A stretchable carbon nanotube strain sensor for human-motion detection // Nat. Nanotechnol. 2011. Vol. 6, № 5. P. 296–301.

70. Gilshteyn E.P. et al. All-nanotube stretchable supercapacitor with low equivalent series resistance // Sci. Rep. 2017. Vol. 7, № 1.

71. Gilshteyn E.P. et al. Mechanically Tunable Single-Walled Carbon Nanotube Films as a Universal Material for Transparent and Stretchable Electronics // ACS Appl. Mater. Interfaces. 2019. Vol. 11, № 30. P. 27327–27334.

72. Talbot, L.Cheng, R. K., Schefer, R. W., & Willis D.R. Thermophoresis of particles in a heated boundary layer // J. Fluid Mech. 1980. Vol. 101, № 4. P. 737–758.

73. Kennard E.H., others. Kinetic theory of gases. McGraw-hill New York, 1938. Vol. 483.

74. Gonzalez D. et al. A new thermophoretic precipitator for collection of nanometer-sized aerosol particles // Aerosol Sci. Technol. 2005. Vol. 39, № 11. P. 1064–

1071.

75.   Laiho P. et al. Dry and Direct Deposition of Aerosol-Synthesized Single-Walled Carbon Nanotubes by Thermophoresis // ACS Appl. Mater. Interfaces. 2017. Vol. 9, № 24. P. 20738–20747.

76.   Kaikkonen J.P. et al. Suspended superconducting weak links from aerosol-synthesized single-walled carbon nanotubes // Nano Res. 2020. Vol. 13, № 12. P. 3433–3438.

77.   Laiho P. et al. Wafer-Scale Thermophoretic Dry Deposition of Single-Walled Carbon Nanotube Thin Films // ACS Omega. 2018. Vol. 3, № 1. P. 1322–1328.

78.   Novikov I. V. et al. Residence time effect on single-walled carbon nanotube synthesis in an aerosol CVD reactor // Chem. Eng. J. Elsevier B.V., 2021. Vol. 420, № P1. P. 129869.

79.   Jovanovic O. Photophoresis-Light induced motion of particles suspended in gas // J. Quant. Spectrosc. Radiat. Transf. 2009. Vol. 110, № 11. P. 889–901.

80.   Horvath H. Photophoresis - A forgotten force?? // KONA Powder Part. J. 2014. Vol. 31, № 1. P. 181–199.

81.   Kataura H. et al. Optical properties of single-wall carbon nanotubes // Synth. Met. 1999. Vol. 103, № 1–3. P. 2555–2558.

82.   Hill E.H. et al. Opto-Thermophoretic Attraction, Trapping, and Dynamic Manipulation of Lipid Vesicles // Langmuir. 2018. Vol. 34, № 44. P. 13252–13262.

83.   Lei H. et al. Photophoretic assembly and migration of dielectric particles and

Escherichia coli in liquids using a subwavelength diameter optical fiber // Lab Chip. 2011. Vol. 11, № 13. P. 2241–2246.

84.	Haisch C., Kykal C., Niessner R. Photophoretic velocimetry for the characterization of aerosols // Anal. Chem. 2008. Vol. 80, № 5. P. 1546–1551.

85.	Helmbrecht C., Niessner R., Haisch C. Photophoretic velocimetry - A new way for the in situ determination of particle size distribution and refractive index of hydrocolloids // Analyst. 2011. Vol. 136, № 9. P. 1987–1994.

86.	Küpper M. et al. Photophoresis on polydisperse basalt microparticles under microgravity // J. Aerosol Sci. Elsevier, 2014. Vol. 76. P. 126–137.

87.	Cruz Garrido A.R., Guzmán Barraza A., Ortega Mendoza J.G. Migration of silver microparticles suspended in water by photophoresis induced with laser radiation. 2020. Vol. 1146318, № August 2020. P. 42.

88.	Monjushiro H., Tanaka M., Watarai H. Periodic Expansion-contraction Motion of Photoabsorbing Organic Droplets during Laser Photophoretic Migration in Water // Chem. Lett. 2003. Vol. 32, № 3. P. 254–255.

89.	Tanaka M., Monjushiro H., Watarai H. Laser photophoretic migration with periodic expansion-contraction motion of photo-absorbing microemulsion droplets in water // Langmuir. 2004. Vol. 20, № 25. P. 10791–10797.

90.	Smith D. et al. Photophoretic separation of single-walled carbon nanotubes: A novel approach to selective chiral sorting // Phys. Chem. Chem. Phys. 2014. Vol. 16, № 11. P. 5221–5228.

91.	Pereira D.J.S., Panão M.R.O. Photophoresis of spherical particles in slip-flow

regime // Phys. Fluids. AIP Publishing LLC, 2022. Vol. 34, № 10.

92. Gopannagari M., Bakaraju V., Chaturvedi H. Photophoresis in single walled carbon nanotubes // Mater. Res. Express. IOP Publishing, 2015. Vol. 2, № 7. P. 75012.

93. Skelton Spesyvtseva S.E., Shoji S., Kawata S. Chirality-Selective Optical Scattering Force on Single-Walled Carbon Nanotubes // Phys. Rev. Appl. 2015. Vol. 3, № 4. P. 1–6.

94. Glerup M. et al. Synthesis of N-doped SWNT using the arc-discharge procedure // Chem. Phys. Lett. 2004. Vol. 387, № 1–3. P. 193–197.

95. Keskar G. et al. Growth, nitrogen doping and characterization of isolated single-wall carbon nanotubes using liquid precursors // Chem. Phys. Lett. 2005. Vol. 412, № 4–6. P. 269–273.

96. Ren W. et al. The Intrinsic Nature of Persulfate Activation and N-Doping in Carbocatalysis // Environ. Sci. Technol. 2020. Vol. 54, № 10. P. 6438–6447.

97. Duan X. et al. Insights into N-doping in single-walled carbon nanotubes for enhanced activation of superoxides: A mechanistic study // Chem. Commun. Royal Society of Chemistry, 2015. Vol. 51, № 83. P. 15249–15252.

98. Ayala P. et al. Tailoring N-doped single and double wall carbon nanotubes from a nondiluted carbon/nitrogen feedstock // J. Phys. Chem. C. 2007. Vol. 111, № 7. P. 2879–2884.

99. Shiraishi S. et al. Electric double layer capacitance of multi-walled carbon nanotubes and B-doping effect // Appl. Phys. A Mater. Sci. Process. 2006. Vol. 82,

№ 4 SPEC. ISS. P. 585–591.

100. Liu X.M., Gutiérrez H.R., Eklund P.C. Electrical properties and far infrared optical conductivity of boron-doped single-walled carbon nanotube films // J. Phys. Condens. Matter. 2010. Vol. 22, № 33.

101. Ayala P. et al. A one step approach to B-doped single-walled carbon nanotubes // J. Mater. Chem. 2008. Vol. 18, № 46. P. 5676–5681.

102. Gai P.L. et al. Structural systematics in boron-doped single wall carbon nanotubes // J. Mater. Chem. 2004. Vol. 14. P. 669–675.

103. Borowiak-Palen E. et al. Efficient production of B-substituted single-wall carbon nanotubes // Chem. Phys. Lett. 2003. Vol. 378, № 5–6. P. 516–520.

104. Li W. et al. Silver-filled single-walled carbon nanotubes: Atomic and electronic structures from first-principles calculations // Phys. Rev. B - Condens. Matter Mater. Phys. 2006. Vol. 74, № 19. P. 1–8.

105. Zhou J. et al. Structural, electronic, and transport properties of Gd/Eu atomic chains encapsulated in single-walled carbon nanotubes // J. Phys. Chem. C. 2010. Vol. 114, № 36. P. 15347–15353.

106. Sun Y., Yang X., Ni J. Bonding differences between single iron atoms versus iron chains with carbon nanotubes: First-principles calculations // Phys. Rev. B - Condens. Matter Mater. Phys. 2007. Vol. 76, № 3. P. 1–8.

107. Kharlamova M. V. Advances in tailoring the electronic properties of single-walled carbon nanotubes // Prog. Mater. Sci. Elsevier Ltd, 2016. Vol. 77. P. 125–211.

108. Kim S.M. et al. Reduction-controlled viologen in bisolvent as an environmentally

stable n-type dopant for carbon nanotubes (J. Am. Chem. Soc. (2009) 131(327-331)) // J. Am. Chem. Soc. 2009. Vol. 131, № 13. P. 5010.

109. Yasunishi T., Kishimoto S., Ohno Y. Effect of ambient air on n-type carbon nanotube thin-film transistors chemically doped with poly(ethylene imine) // Jpn. J. Appl. Phys. 2014. Vol. 53, № 5 SPEC. ISSUE 1. P. 2–7.

110. Dai R. et al. Adjustable hydrazine modulation of single-wall carbon nanotube network field effect transistors from p-type to n-type // Nanotechnology. IOP Publishing, 2016. Vol. 27, № 44. P. 1–7.

111. Xu J.L. et al. Efficient and Reversible Electron Doping of Semiconductor-Enriched Single-Walled Carbon Nanotubes by Using Decamethylcobaltocene // Sci. Rep. Springer US, 2017. Vol. 7, № 1. P. 1–10.

112. Hussain A. et al. Floating catalyst CVD synthesis of single walled carbon nanotubes from ethylene for high performance transparent electrodes // Nanoscale. Royal Society of Chemistry, 2018. Vol. 10, № 20. P. 9752–9759.

113. Rajanna P.M. et al. Rational design of highly efficient flexible and transparent p-type composite electrode based on single-walled carbon nanotubes // Nano Energy. Elsevier Ltd, 2019. Vol. 67. P. 104183.

114. Kim K.K. et al. Doping strategy of carbon nanotubes with redox chemistry // New J. Chem. 2010. Vol. 34, № 10. P. 2183–2188.

115. Peter Chen I.W. et al. Highly conductive carbon nanotube buckypapers with improved doping stability via conjugational cross-linking // Nanotechnology. 2011. Vol. 22, № 48. P. 485708.

116. D'Arsié L. et al. Stable, efficient p-type doping of graphene by nitric acid // RSC Adv. 2016. Vol. 6, № 114. P. 113185–113192.

117. Hellstrom S.L. et al. Strong and stable doping of carbon nanotubes and graphene by MoO x for transparent electrodes // Nano Lett. 2012. Vol. 12, № 7. P. 3574–3580.

118. Zhu Y. et al. Rational design of hybrid graphene films for high-performance transparent electrodes // ACS Nano. 2011. Vol. 5, № 8. P. 6472–6479.

119. Kim S.H. et al. Carbon nanotube and graphene hybrid thin film for transparent electrodes and field effect transistors // Adv. Mater. 2014. Vol. 26, № 25. P. 4247–4252.

120. Kim K.K., Kim S.M., Lee Y.H. Chemically Conjugated Carbon Nanotubes and Graphene for Carrier Modulation // Acc. Chem. Res. 2016. Vol. 49, № 3. P. 390–399.

121. Tian Y. et al. Bilayer and three dimensional conductive network composed by SnCl2 reduced rGO with CNTs and GO applied in transparent conductive films // Sci. Rep. Nature Publishing Group UK, 2021. Vol. 11, № 1. P. 1–12.

122. Wang T. et al. Strong adhesion and high optoelectronic performance hybrid graphene/carbon nanotubes transparent conductive films for green-light OLED devices // Surfaces and Interfaces. Elsevier B.V., 2021. Vol. 24, № December 2020. P. 101137.

123. Gorkina A.L. et al. Transparent and conductive hybrid graphene/carbon nanotube films // Carbon N. Y. Elsevier Ltd, 2016. Vol. 100. P. 501–507.

124. Zhu Z.R. et al. Highly transparent, low sheet resistance and stable Tannic acid modified-SWCNT/AgNW double-layer conductive network for organic light emitting diodes // Nanotechnology. 2021. Vol. 32, № 1.

125. Bogdanova A.R., Krasnikov D. V., Nasibulin A.G. The role of sulfur in the CVD carbon nanotube synthesis // Carbon N. Y. Pergamon, 2023. Vol. 210. P. 118051.

126. Reynaud O. et al. Aerosol feeding of catalyst precursor for CNT synthesis and highly conductive and transparent film fabrication // Chem. Eng. J. Elsevier B.V., 2014. Vol. 255. P. 134–140.

127. Khabushev E.M. et al. Joint effect of ethylene and toluene on carbon nanotube growth // Carbon N. Y. Elsevier Ltd, 2022. Vol. 189. P. 474–483.

128. Knudsen M. Die molekulare Wärmeleitung der Gase und der Akkommodationskoeffizient // Ann. Phys. 1911. Vol. 339, № 4. P. 593–656.

129. Hettner G. Zur Theorie der Photophorese // Zeitschrift für Phys. 1926. Vol. 37, № 3. P. 179–192.

130. Rohatschek H. Semi-empirical model of photophoretic forces for the entire range of pressures // J. Aerosol Sci. 1995. Vol. 26, № 5. P. 717–734.

131. Yalamov Y.I., Kutukov V.B., Shchukin E.R. Theory of the photophoretic motion of the large-size volatile aerosol particle // J. Colloid Interface Sci. 1976. Vol. 57, № 3. P. 564–571.

132. Mackowski D.W. Photophoresis of aerosol particles in the free molecular and slip-flow regimes // Int. J. Heat Mass Transf. 1988. Vol. 32, № 5. P. 843–854.

133. Keh H.J., Tu H.J. Thermophoresis and photophoresis of cylindrical particles //

Colloids Surfaces A Physicochem. Eng. Asp. 2001. Vol. 176, № 2–3. P. 213–223.

134. Chang Y.C., Keh H.J. Thermophoresis and photophoresis of an aerosol cylinder with thermal stress slip // Am. J. Heat Mass Transf. 2017. Vol. 4, № 2. P. 85–103.

135. Erokhin A. V. et al. Phenylacetylene hydrogenation on Fe@C and Ni@C core-shell nanoparticles: About intrinsic activity of graphene-like carbon layer in H2 activation // Carbon N. Y. Elsevier Ltd, 2014. Vol. 74, № Cvd. P. 291–301.

136. Nishihara T. et al. Empirical formulation of broadband complex refractive index spectra of single-chirality carbon nanotube assembly // Nanophotonics. 2022. Vol. 11, № 5. P. 1011–1020.

137. Tabakman S.M. et al. Optical properties of single-walled carbon nanotubes separated in a density gradient: Length, bundling, and aromatic stacking effects // J. Phys. Chem. C. 2010. Vol. 114, № 46. P. 19569–19575.

138. O'Connell M.J. et al. Band gap fluorescence from individual single-walled carbon nanotubes // Science (80-.). 2002. Vol. 297, № 5581. P. 593–596.

139. Appenzeller J. Carbon nanotubes for high-performance electronics - Progress and prospect // Proc. IEEE. 2008. Vol. 96, № 2. P. 201–211.

140. Gotthardt J.M. et al. Molecular n-Doping of Large- And Small-Diameter Carbon Nanotube Field-Effect Transistors with Tetrakis(tetramethylguanidino)benzene // ACS Appl. Electron. Mater. 2021. Vol. 3, № 2. P. 804–812.

141. Weisman R.B. Fluorimetric characterization of single-walled carbon nanotubes // Anal. Bioanal. Chem. 2010. Vol. 396, № 3. P. 1015–1023.

142. Barone P.W. et al. Near-infrared optical sensors based on single-walled carbon

nanotubes // Nat. Mater. 2005. Vol. 4, № 1. P. 86–92.

143. Jeantet A. et al. Widely Tunable Single-Photon Source from a Carbon Nanotube in the Purcell Regime // Phys. Rev. Lett. 2016. Vol. 116, № 24. P. 1–5.

144. Zavodchikova M.Y. et al. Carbon nanotube thin film transistors based on aerosol methods // Nanotechnology. 2009. Vol. 20, № 8.

145. Greiner M.T. et al. Transition metal oxide work functions: The influence of cation oxidation state and oxygen vacancies // Adv. Funct. Mater. 2012. Vol. 22, № 21. P. 4557–4568.

146. Meyer J. et al. Transition metal oxides for organic electronics: Energetics, device physics and applications // Adv. Mater. 2012. Vol. 24, № 40. P. 5408–5427.

147. Chenakin S.P., Silvy R.P., Kruse N. Effect of X-rays on the surface chemical state of Al2O 3, v2O5, and aluminovanadate oxide // J. Phys. Chem. B. 2005. Vol. 109, № 30. P. 14611–14618.

148. Gauntt B.D., Dickey E.C., Horn M.W. Stoichiometry and microstructural effects on electrical conduction in pulsed dc sputtered vanadium oxide thin films // J. Mater. Res. 2009. Vol. 24, № 4. P. 1590–1599.

149. Livage J. Vanadium Pentoxide Gels // Chem. Mater. 1991. Vol. 3, № 4. P. 578–593.

150. Özer N. Electrochemical properties of sol-gel deposited vanadium pentoxide films // Thin Solid Films. 1997. Vol. 305, № 1–2. P. 80–87.

151. Q. Wen, Jhin-Fang Huang, L.-Y. Cao J.-P.W. Preparation and synthesized activation energy of V2O5 microcrystallites synthesized by sol-gel method // J.

Synth. Cryst. 2011. Vol. 40, № 5. P. 1242–1245.

152. D'elia A. et al. Interplay among work function, electronic structure and stoichiometry in nanostructured VO: X films // Phys. Chem. Chem. Phys. 2020. Vol. 22, № 11. P. 6282–6290.

153. Tsapenko A.P. et al. Aerosol-Assisted Fine-Tuning of Optoelectrical Properties of SWCNT Films // J. Phys. Chem. Lett. 2019. Vol. 10, № 14. P. 3961–3965.

154. Glukhova O.E., Shmygin D.S. The electrical conductivity of CNT/graphene composites: A new method for accelerating transmission function calculations // Beilstein J. Nanotechnol. 2018. Vol. 9, № 1. P. 1254–1262.

155. Jeon I., Matsuo Y., Maruyama S. Single-Walled Carbon Nanotubes in Solar Cells // Top. Curr. Chem. Springer International Publishing, 2018. Vol. 376, № 1. P. 1–28.

156. White C.T., Todorov T.N. Carbon nanotubes as long ballistic conductors // Nature. 1998. Vol. 393, № 6682. P. 240–241.